Light-activated nanoclusters with tunable ROS for wound infection treatment

Xin Wang [a,1], Jianing Ding [a,1], Xiao Chen [b,c,d,1], Sicheng Wang [c,d,e,1], Zhiheng Chen [a], uanyuan Chen [a], Guowang Zhang [a], Ji Liu [a], Tingwang Shi [a], Jian Song [b], Shihao Sheng [b], Guangchao Wang [b], Jianguang Xu [a,****], Jiacan Su [b,c,d,f,***], Wei Zhang [a,**], Xiaofeng Lian [a,*]

[a] *Department of Orthopedic Surgery, Shanghai Sixth People's Hospital Affiliated to Shanghai Jiao Tong University School of Medicine, Shanghai, 200233, China*
[b] *Department of Orthopaedics, Xinhua Hospital Affiliated to Shanghai JiaoTong University School of Medicine, Shanghai, 200092, China*
[c] *Institute of Translational Medicine, Shanghai University, Shanghai, 200444, China*
[d] *Organoid Research Center, Shanghai University, Shanghai, 200444, China*
[e] *Department of Orthopedics Trauma, Shanghai Zhongye Hospital, Shanghai, 200941, China*
[f] *National Center for Translational Medicine (Shanghai) SHU Branch, Shanghai University, Shanghai, 200444, China*

ARTICLE INFO

ABSTRACT

Infected wounds pose a significant clinical challenge due to bacterial resistance, recurrent infections, and impaired healing. Reactive oxygen species (ROS)-based strategies have shown promise in eradicating bacterial infections. However, the excess ROS in the infection site after treatments may cause irreversible damage to healthy tissues. To address this issue, we developed bovine serum albumin-iridium oxide nanoclusters (BSA-IrO$_x$ NCs) which enable photo-regulated ROS generation and scavenging using near infrared (NIR) laser. Upon NIR laser irradiation, BSA-IrO$_x$ NCs exhibit enhanced photodynamic therapy, destroying biofilms and killing bacteria. When the NIR laser is off, the nanoclusters' antioxidant enzyme-like activities prevent inflammation and repair damaged tissue through ROS clearance. Transcriptomic and metabolomic analyses revealed that BSA-IrO$_x$ NCs inhibit bacterial nitric oxide synthase, blocking bacterial growth and biofilm formation. Furthermore, the nanoclusters repair impaired skin by strengthening cell junctions and reducing mitochondrial damage in a fibroblast model. In vivo studies using rat infected wound models confirmed the efficacy of BSA-IrO$_x$ NCs. This study presents a promising strategy for treating biofilm-induced infected wounds by regulating the ROS microenvironment, addressing the challenges associated with current ROS-based antibacterial approaches.

1. Introduction

Infected wound management remains a major clinical challenge [1], as prolonged bacterial invasion can lead to tissue necrosis, suppuration, and, in severe cases, amputation [2]. Current clinical treatments for wound infections often involve fungicides like iodophor or antibiotics for cleansing and sterilization [3,4]. However, fungicides fail to eliminate all bacteria within the tissue, and the widespread use of antibiotics has resulted in bacterial resistance, hindering the healing process of infected wounds [5–7]. Therefore, from a clinical perspective, an effective therapeutic strategy that combines infected wound sterilization with tissue repair is of utmost importance.

Reactive oxygen species (ROS) play a crucial role in disinfection as they can destroy bacterial cell membranes and DNA, triggering an

inflammatory response that ultimately leads to the death of bacteria and biofilms [8,9]. Among the most developed ROS-based bactericidal techniques, including chemodynamic therapy [10], sonodynamic therapy [11], and photodynamic treatment (PDT) [12], PDT has the greatest clinical potential due to its ability to generate larger amounts of ROS more rapidly and efficiently [13–15]. Although PDT has been effectively used in clinical settings for treating periodontal and wound infections, excessive ROS can exacerbate tissue damage at the infection site by activating inflammation and producing inflammatory factors such as interleukin-1β (IL-1β), IL-6, and tumor necrosis factor-α (TNF-α) [16, 17]. While nanoparticle-based treatment platforms can counteract ROS damage through their inherent tissue repair properties, they are unable to scavenge the excess ROS generated by PDT, leading to chronic inflammation [18]. Therefore, developing strategies to scavenge excess ROS in tissues after PDT is crucial for the effective treatment of infected wounds.

Scavenging ROS and reducing inflammation can promote cell proliferation in wounds, thereby initiating tissue repair [19,20]. Moreover, ROS bursts are the primary cause of mitochondrial damage [21]. Rapid increases in ROS disrupt mitochondrial structure, inhibit mitochondrial division and autophagy, and obstruct mitochondrial self-repair [22,23]. Consequently, scavenging ROS in tissues significantly enhances cellular mitochondrial function by reducing mitochondrial damage and promoting mitochondrial division, providing sufficient energy for tissue restoration [24,25].

Recent studies have primarily focused on ROS generation for combating bacteria. However, it is critical to employ effective strategies to regulate both the generation and sequestration of ROS to effectively alleviate wound infections. Due to their many advantages, including good biocompatibility, mild reaction conditions, and robust stability, albumin-based mineralized nanomaterials have gained wide attention in biomedical applications [26]. Bovine serum albumin (BSA), the most commercially available protein, has been extensively used as a bio-template to form protein-coated metal oxide nanoclusters through a gentle biomineralization method [27,28]. As a representative nanomaterial, the albumin-based mineralized iridium nanomaterial has been explored [29]. The PDT effect of iridium oxide can be achieved with an NIR laser. Additionally, its good catalytic activity and multi-enzyme activities have been considered and demonstrated [30]. Thus, there is a great need to explore the potential of Ir-based nanomaterials for ROS regulation in infected wound management.

In this work, we propose the use of BSA–iridium oxide (BSA-IrO$_x$) nanoclusters (NCs) for the treatment of infected wounds through the controllable regulation of ROS levels at the infection site (**Graphical Abstract**). The photosensitizing property of IrO$_x$ enables highly efficient generation of $^1O_2$ upon irradiation with an 808 nm near-infrared (NIR) laser, resulting in potent antibacterial effects. When the NIR laser is turned off, the multiple enzyme-like activities (e.g., catalase-like (CAT), superoxide dismutase (SOD), and hydroxyl radical scavenging) of the BSA-IrO$_x$ NCs rapidly scavenge excessive ROS, thereby avoiding inflammatory responses at the wound site, reducing irreversible damage to healthy tissues, and increasing cell junctions. Furthermore, oxygen consumption and ATP detection tests demonstrated that BSA-IrO$_x$ NCs enhance mitochondrial function, further promoting the restoration of damaged tissues. The therapeutic efficacy of these agents was validated in rat models in vivo and human fibroblast models in vitro. In conclusion, BSA-IrO$_x$ NCs effectively modulate the ROS microenvironment through NIR laser control, enabling the treatment and prevention of infected wounds, thus showing great potential for future clinical applications.

2. Results and discussion

2.1. Preparation and characterization of BSA-IrO$_x$ NCs

BSA-IrO$_x$ NCs were synthesized through a biomineralization process

according to methods described in previous studies [31]. Transmission electron microscopy (TEM) images demonstrated that the as-obtained BSA-IrO$_x$ aggregated to form particles with a size of 48 ± 5.3 nm (Fig. 1A). The nanoclusters are composed of numerous small granulums with the size of 1.3 ± 0.3 nm, thus called nanoclusters. The elemental mapping indicated that O, N, Ir, and S were present, thus confirming the successful preparation of the BSA-IrO$_x$ NCs. In addition, the elemental composition of the NCs was further confirmed by X-ray Photoelectron Spectroscopy (XPS) (Fig. 1B). The characteristic peaks of the high-resolution spectrum of Ir 4f were attributed to Ir 4f $_{7/2}$ (62.3 eV) and Ir 4f $_{5/2}$ (65.17 eV), and the O 1 s peaks were centered at the deconvoluted peaks at 533.01 and 531.47 eV, which are attributed to the –C═O (BSA), and Ir–O–Ir bonding, respectively (Fig. 1C and D) [32]. The hydrodynamic size of the BSA-IrO$_x$ NCs was ≈58.8 nm (Fig. 1E), and the zeta potential was −36.25 ± 3.94 mV (Fig. S1). The Fourier transform infrared spectroscopy spectrum characterizations of BSA-IrO$_x$ was further evaluated (Fig. S2). The characteristic bands at about 1655 and 1540 cm^{-1} of BSA-IrO$_x$ NCs were consistent with those of bare BSA, confirming the BSA coating. Moreover, the X-ray powder diffraction (XRD) spectrum displays a broad peak (Fig. S3), indicating the designed BSA-IrO$_x$ NCs were amorphous. Inductively coupled plasma-optical emission spectroscopy (ICP-OES) measurements determined the concentration of Ir in the NCs to be 406 μg/ml. These characterization results demonstrate the successful synthesis of BSA-IrOx NCs with well-defined physicochemical properties, which are essential for their therapeutic performance, as outlined in **Graphical Abstract**.

We investigated the PDT effects of BSA-IrO$_x$ NCs under NIR laser irradiation. Electron spin resonance spectroscopy (ESR) revealed that BSA-IrO$_x$ NCs could produce a large amount of singlet oxygen ($^1O_2$) under an 808 nm NIR laser (Fig. 1F). The $^1O_2$ production by PDT was further confirmed using a 1,3-Diphenylisobenzofuran (DPBF) probe. When $^1O_2$ is present, DPBF can quickly capture it and combine with it, resulting in a reduction of the absorbance of DPBF at 412 nm. This reduction can indirectly reflect the ability of porphyrin compounds to produce $^1O_2$. The results showed increased fluorescence with increasing concentrations of BSA-IrO$_x$ NCs (Fig. S4). Interestingly, when the NIR laser was withdrawn, the BSA-IrO$_x$ NCs scavenged various types of ROS, including H$_2$O$_2$, hydroxyl radicals (•OH), and superoxide anions (•O$_2^-$). ESR analysis verified the hydroxyl radical scavenging ability of the BSA-IrO$_x$ NCs, which convert •OH into H$_2$O and O$_2$ (Fig. 1G). Similarly, ESR analysis confirmed the SOD-like function of the BSA-IrO$_x$ NCs, converting •O$_2^-$ into O$_2$ and H$_2$O$_2$ (Fig. 1H). Furthermore, the H$_2$O$_2$ decomposition curve demonstrated that the BSA-IrO$_x$ NCs decomposed a large amount of H$_2$O$_2$ through a catalase (CAT)-like process (Fig. 1I). These experiments establish that BSA-IrO$_x$ NCs promote ROS generation and scavenging through an NIR laser switch, providing a foundation for their therapeutic applications.

There are three types of ROS commonly found in the human body, including $^1O_2$, •OH, and •O$_2^-$, which play important roles in the progression of inflammation [33]. BSA-IrO$_x$ NCs can decompose different kinds of ROS through CAT, SOD, and hydroxyl radical scavenging activities, thereby more comprehensively inhibiting inflammation in tissues. Experimental results show that the ability of BSA-IrO$_x$ NCs to decompose ROS is positively correlated with its concentration, indicating its excellent enzyme activity and clinical therapeutic potential.

2.2. In vitro antibacterial and antibiofilm effects of BSA-IrO$_x$ NCs with NIR irradiation

The photothermal effect of BSA-IrO$_x$ NCs was inhibited to explore their PDT effect. All bacterial experiments were conducted in a constant-temperature water bath, maintaining the temperature of the bacterial medium below 43 °C (Fig. S5). We also plotted the bacterial culture curve under photothermal therapy (PTT) after 10 min of NIR laser exposure (Fig. S6). However, this study focused on changes in ROS levels, so we chose to culture bacteria at a temperature of no more than
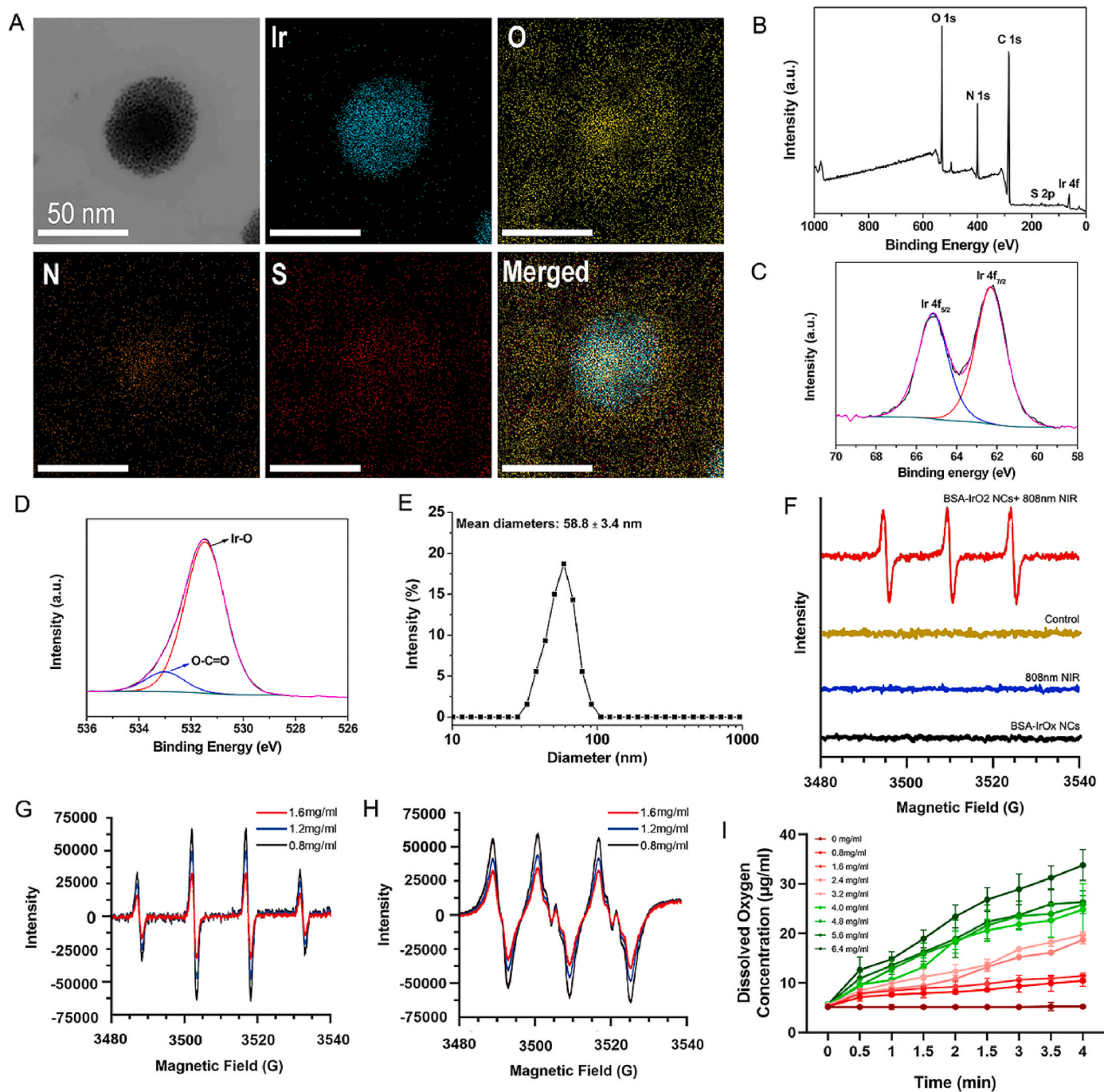
Fig. 1. Preparation and characterization of BSA-IrO$_x$ NCs.
A. TEM image and the elemental mappings of BSA-IrO$_x$ NCs. B. XPS spectrum of the BSA-IrO$_x$ NCs. XPS high-resolution spectrum of (C) Ir 4f and (D) O 1s. E. Hydrodynamic size of the BSA-IrO$_x$ NCs. F. ESR spectra of the reaction systems after various treatments using TEMP as the spin trap. ESR spectra of $^1O_2$ under 808 nm NIR laser irradiation with BSA-IrO$_x$ NCs in TEMP solution. (G) •OH and (H) •O$_2^-$ scavenging ability of BSA-IrO$_x$ NCs by ESR spectrum analysis. I. Oxygen concentration curve after mixing different concentrations of BSA-IrO$_x$ NCs with H$_2$O$_2$.

43 °C under NIR irradiation for 5 min. This approach allowed us to specifically study the effect of PDT. The in vitro antibacterial effect of BSA-IrO$_x$ NCs was evaluated using methicillin-resistant Staphylococcus aureus (MRSA). The bacterial survival rate significantly decreased with increasing BSA-IrO$_x$ NCs concentration when the bacterial suspension was coincubated with BSA-IrO$_x$ NCs for 2 h, indicating concentration-dependent antibacterial activity (Fig. 2A). The time-dependent OD600 curve showed that BSA-IrO$_x$ NCs + NIR significantly affected bacterial reproduction over time (Fig. 2B), with strong inhibition at concentrations greater than 1.6 mg/ml, suggesting a minimum inhibitory

concentration of 1.6 mg/ml. A bacterial coating test revealed a minimum bactericidal concentration of 4.8 mg/ml for BSA-IrO$_x$ NCs.

The in vitro antibiofilm activity of BSA-IrO$_x$ NCs was evaluated using standard plate tests (Fig. 2C), which showed a 0.28 lg CFU/mL reduction in MRSA viability (46.72 % antibiofilm efficiency) for BSA-IrO$_x$ NCs + NIR treatment. The bacterial activity of the BSA-IrO$_x$ + NIR group decreased by 2.47 log CFU/mL, indicating an antibacterial rate of 99.66 %. The antibacterial ability of commonly used Ag$^+$ nanoparticles (NPs) was 99.06 %, with no significant difference between the two. This result indicates that BSA-IrO$_x$ NCs have excellent clinical anti-infection
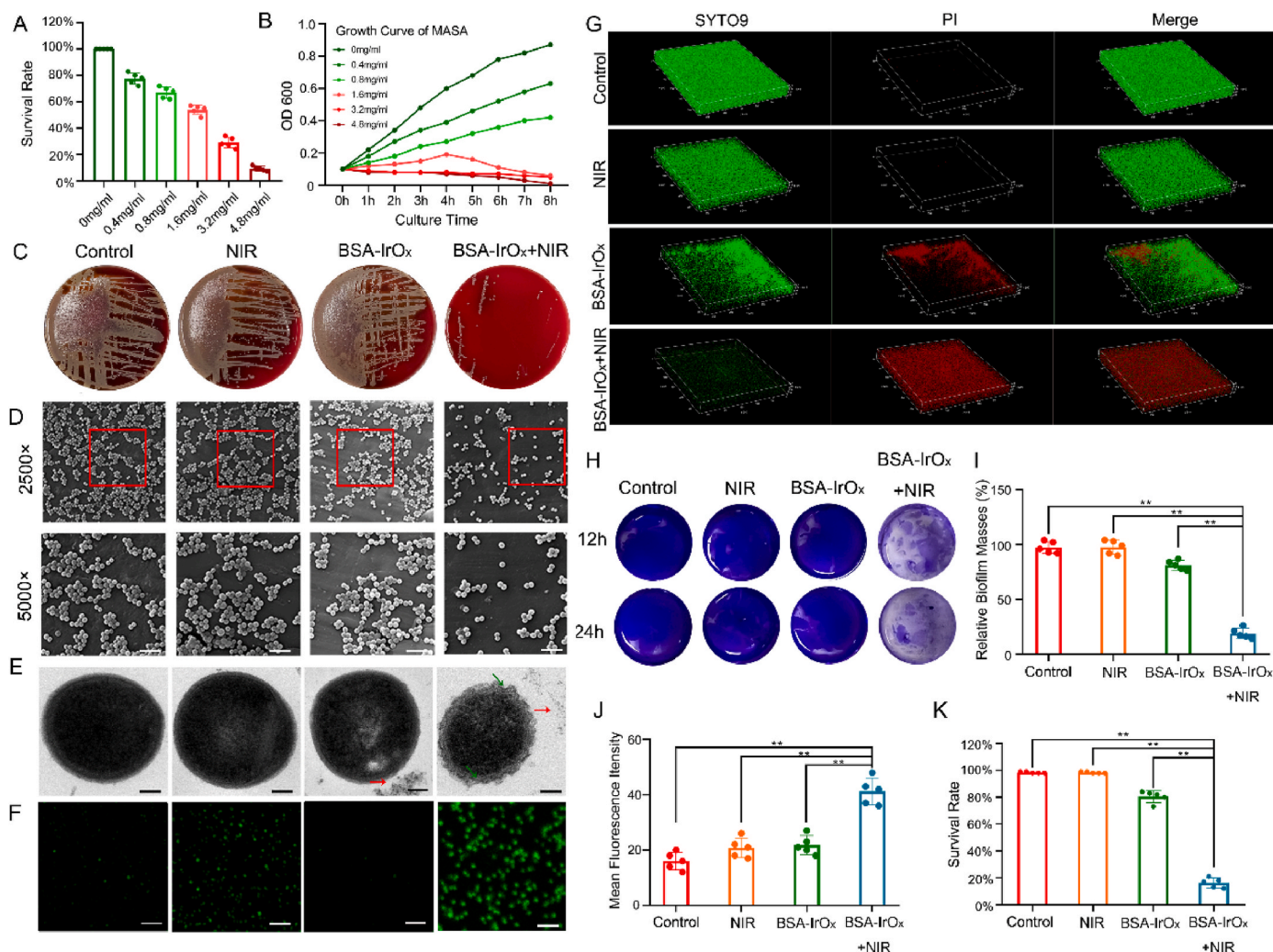
Fig. 2. BSA-IrO$_x$ NCs + NIR sterilize and disrupt biofilms in vitro.
A. Survival rate of MRSA with different concentrations of BSA-IrO$_x$ NCs. B. Time-dependent curve of MRSA in BSA-IrO$_x$ + NIR group. C. Standard plate tests of the different treatments. D. Representative SEM images of MRSA after different treatments, scale bar: 5 μm. E. Representative TEM images of MRSA after different treatments, scale bar: 0.2 μm. F. DFPH fluorescence analysis of ROS in MRSA after different treatments, scale bar: 5 μm. G. Representative CLSM images of the LIVE-DEAD staining after different treatments. H. Crystal violet staining of bacterial biofilms after different treatments. I. Statistical results of crystal violet staining of biofilms after different treatments, ** represents $p < 0.01$, n = 5. J. Red fluorescence analysis of the biofilms CLSM after different treatments, ** represents $p < 0.01$, n = 5. K. Counts of live bacteria of the bacterial biofilms after different treatments, ** represents $p < 0.01$, n = 5.

potential [34]. Biological scanning electron microscopy (SEM) clearly revealed MRSA agglutination, significantly reduced bacterial numbers, and destroyed biofilms in the BSA-IrO$_x$ + NIR group (Fig. 2D). These results demonstrate the potent antibacterial and antibiofilm effects of BSA-IrO$_x$ NCs under NIR irradiation.

Next, we first studied the effect of NIR with different intensities and irradiation times on the antibacterial effect. The results showed that the higher the intensity of NIR and the longer the irradiation time, the better the antibacterial effect (Fig. S7). To reduce tissue damage, we chose to conduct experiments under 4 mW/cm^2 NIR laser for 5 min, which can effectively inhibit bacterial growth. To further clarify the antibacterial efficacy and clinical therapeutic potential of BSA-IrO$_x$ NCs + NIR, we compared them with Ag$^+$ NPs, which are clinically used, and the classical antibiotic vancomycin. The results showed that the antibacterial performance of BSA-IrO$_x$ + NIR was slightly inferior to that of Ag$^+$ NPs, but there was no significant difference between them. The antibacterial activity of vancomycin was significantly stronger than that of both nanomaterials. Notably, the combination of BSA-IrO$_x$ NCs + NIR and vancomycin enhanced the effect of vancomycin to a certain extent, which opens new possibilities for the clinical application of BSA-IrO$_x$

NCs (Fig. S8).

The effectiveness of BSA-IrO$_x$ NCs against planktonic bacteria was confirmed through the above experiments. Biological TEM revealed the morphology of individual bacteria. The addition of BSA-IrO$_x$ NCs alone did not significantly change the bacterial morphology, as indicated by the red arrow (Fig. 2E). However, in the BSA-IrO$_x$ + NIR group, the outer membrane of the MRSA cells was disrupted (shown by the green arrow), and the cytoplasm appeared non-uniform, which is a significant manifestation of ROS-induced damage. To clarify the ROS production by BSA-IrO$_x$ NCs + NIR, the ROS levels in each biofilm group were determined using 2′,7′-dichlorodihydrofluorescein diacetate (DCFH-DA). The control group showed no obvious green fluorescence, indicating low ROS levels. In contrast, the BSA-IrO$_x$ NCs + NIR samples emitted a high amount of green fluorescence, suggesting accelerated ROS production due to hyperthermia (Fig. 2F). The fluorescence intensity decreased significantly in the BSA-IrO$_x$ group, attributed to ROS clearance. In summary, PDT via BSA-IrO$_x$ NCs under NIR laser irradiation produces ROS, as verified by DPBF detection. SEM and TEM analyses demonstrated that BSA-IrO$_x$ NCs destroyed the bacterial cell wall and membrane, thereby reducing the number of bacteria. These findings establish

the bactericidal effects of BSA-IrO$_x$ NCs through ROS-mediated mechanisms.

2.3. In vitro antibiofilm activity of BSA-IrO$_x$ NCs

Bacterial metabolic pathways spontaneously shift towards anaerobic glycolysis, leading to increased H$_2$O$_2$ concentrations in the biofilm microenvironment, which promotes the generation of ROS-associated inflammatory responses [35]. To visualize the role of nanomaterials in disrupting biofilm formation, SEM was employed to observe changes in bacterial morphology and density after treatment. Compared to the control group, the distribution of bacterial cells after BSA-IrO$_x$ NCs + NIR treatment was sparser. Simultaneous treatment with BSA-IrO$_x$ NCs + NIR significantly decreased the number of attached bacteria, with a considerable number of bacteria suffering irreversible damage, including deformation, perforation, and fragmentation. These findings suggest that BSA-IrO$_x$ NCs can effectively inhibit biofilm formation by altering bacterial morphology and reducing bacterial density through ROS-mediated mechanisms.

Confocal laser scanning microscopy (CLSM) and crystal violet staining were used to qualitatively and quantitatively assess the residual biofilm biomass of all samples. The control group sample was completely covered by dense green biofilm structures with almost no red signal (Fig. 2G and I). In the NIR and BSA-IrO$_x$ groups, a slight redshift and irregular voids of varying sizes were observed, indicating partial depolymerization of biofilm segments from the substrate. The residual biomass was 99.73 % and 82.31 %, respectively. The BSA-IrO$_x$ + NIR group exhibited a more prominent red fluorescence signal compared to the other groups, with a biofilm biomass of 23.42 %. Crystal violet staining (Fig. 2H–J, and K) revealed similar results, with 100 %, 99.21 %, 83.54 %, and 17.42 % of the control group, NIR group, BSA-IrO$_x$ group, and BSA-IrO$_x$ + NIR group, respectively. These findings indicate that BSA-IrO$_x$ NCs + NIR can inhibit biofilm formation and disrupt existing biofilms, attributed to the large amount of ROS produced by NIR laser irradiation. In addition, the BSA-IrO$_x$ NCs group exhibited a certain degree of biofilm damage. This may be because BSA-IrO$_x$ NCs, as a nanomaterial, physically penetrate the biofilm after being added to the bacterial medium, leading to partial biofilm destruction. Bacterial resistance is primarily related to the protective effects of biofilms [36], which not only prevent the entry of antibacterial substances but also slow bacterial metabolism, leading to infection recurrence [37,38]. Our results indicate that BSA-IrO$_x$ NCs + NIR can not only kill MRSA by producing ROS but also reduce the possibility of infection recurrence by inhibiting bacterial adhesion, preventing biofilm formation, and destroying the biofilm structure. By forming a therapy nanoplatform, BSA-IrO$_x$ NCs can treat MASA infection from multiple angles.

2.4. BSA-IrO$_x$ NCs inhibit NOS of MRSA

To further elucidate the effect of BSA-IrO$_x$ NCs on MRSA metabolism, metabolomics analysis and transcriptome sequencing were conducted on BSA-IrO$_x$ NCs + NIR-treated MRSA, followed by combined multiomics analysis. Pearson correlation analysis assessed the reproducibility of sample data within the cohort. The Pearson coefficient within the group was close to 1, significantly greater than that between the groups, indicating high metabolite stability (Figs. S9 and S10). At the same time, the Total Ion Chromatogram (TIC) overlay diagram and intensity distribution can also reflect that the sample is stable enough for detection to be significant (Figs. S11 and S12). Compared to the control group, 1563 metabolites (collectively defined as differentially abundant metabolites) exhibited upregulated expression, while 1016 metabolites exhibited downregulated expression in the BSA-IrO$_x$ + NIR group. Differentially abundant metabolites related to MRSA polarization were selected and displayed in a heatmap (Fig. 3A), volcano map, and Z score (Figs. S13 and S14). The gene expression profile of MRSA was visualized on a volcano plot (Fig. 3B), revealing 1563 upregulated and 1016

downregulated genes in the BSA-IrO$_x$ + NIR group compared to the control. Among the downregulated genes, several prominent genes, including glnA, gltD, and cynT [39], were closely related to bacterial arginine metabolism. Kyoto Encyclopedia of Genes and Genomes (KEGG) enrichment analysis of the metabolomics results (Fig. 3C) and combined KEGG analysis of metabolomic and transcriptomic data (Fig. 3D) revealed that arginine biosynthesis metabolism is central to the effect of BSA-IrO$_x$ NCs + NIR on bacteria.

According to the KEGG analysis (Fig. 3D), arginine synthesis and metabolism, which are important components of the bacterial urea cycle, play crucial roles in bacterial reproduction and biofilm formation under physiological conditions and are the main molecular pathways affected by the antibacterial effect of BSA-IrO$_x$ NCs + NIR. Nitric oxide synthase (NOS), a key rate-limiting enzyme involved in arginine metabolism, converts arginine to NO and citrulline, which is the primary pathway for endogenous NO synthesis in bacteria [40]. Endogenous NO is essential for bacterial resistance to ROS and promotes bacterial survival and proliferation [41]. Studies have shown that NOS inhibition suppresses S. aureus metabolism and proliferation and destroys biofilms [42]. NOS is a crucial enzyme in bacterial NO-related metabolism, producing endogenous NO to inhibit oxidative stress and increasing the synthesis of extracellular matrix-related proteins to promote biofilm maturation. Inhibiting NOS in MRSA significantly reduces the ability to infect and form biofilms and greatly decreases antibiotic resistance. Based on the combined KEGG analysis of metabolomic and transcriptomic data, we hypothesized that BSA-IrO$_x$ NCs enhance bactericidal efficacy by increasing ROS levels through the inhibition of bacterial NOS activity.

RT–PCR analysis was performed to verify several genes with significantly different RNA levels in the transcriptomics experiment. After treatment with BSA-IrO$_x$ NCs + NIR, there were significant differences in the transcription of glnA, gltD, and cynT in MRSA, as well as in the transcription of biofilm-associated proteins (Bap) and NOS, two genes related to endogenous NO [43] (Fig. S15). To determine the effect of BSA-IrO$_x$ NCs on NOS in MRSA, we used kits to detect NOS activity and endogenous NO content in bacteria (Fig. S16). The results showed that BSA-IrO$_x$ NCs could inhibit the NOS activity of bacteria, thus reducing the production of NO in bacteria. Endogenous NO is an important factor in bacterial resistance to ROS and plays a crucial role in MRSA's resistance to PDT. Additionally, NOS activity can affect the bacterial cytochrome enzyme (Cyt), thus impacting the aerobic respiration intensity of bacteria. We tested the activity of Cyt and found that its function decreased (Fig. S17). Oxygen consumption rate (OCR) measurements of MRSA showed that BSA-IrOx NCs inhibited the aerobic respiratory intensity of bacteria (Fig. S18). Cyt not only generates energy through the respiratory chain but also enhances bacterial vitality and the ability to form biofilms [44]. The inhibitory effect of BSA-IrO$_x$ NCs on NOS and Cyt in MRSA can inhibit bacterial activity and enhance the killing effect of PDT on ROS, revealing the three-dimensional antibacterial strategy of BSA-IrO$_x$ NCs.

In this study, a combination of transcriptomics and metabolomics analysis was used to fully and comprehensively understand the transcription and metabolism inside bacteria and more accurately predict the targets of BSA-IrO$_x$ NCs. As a prokaryotic organism, metabolites play a key role in the metabolism of bacteria. However, there is no strict correspondence between metabolites and transcribed mRNA, so this study selected both omics for joint analysis and ultimately identified the relevant mechanism of BSA-IrO$_x$ NCs in promoting PDT.

To clarify the inhibitory effect of BSA-IrO$_x$ NCs on the NOS activity of MRSA, foreign NOS was added after BSA-IrO$_x$ NCs + NIR treatment to recover NOS activity. The addition of NOS increased the survival rate of MRSA compared to BSA-IrO$_x$ NCs + NIR treatment (Fig. 3E), indicating that NOS can initially reduce the bactericidal effect of BSA-IrO$_x$ NCs. Crystal violet staining of the biofilm confirmed that BSA-IrO$_x$ NCs + NIR prevented biofilm formation by inhibiting the NOS activity of MRSA (Fig. 3F). CLSM results showed that the damaged MRSA biofilm was
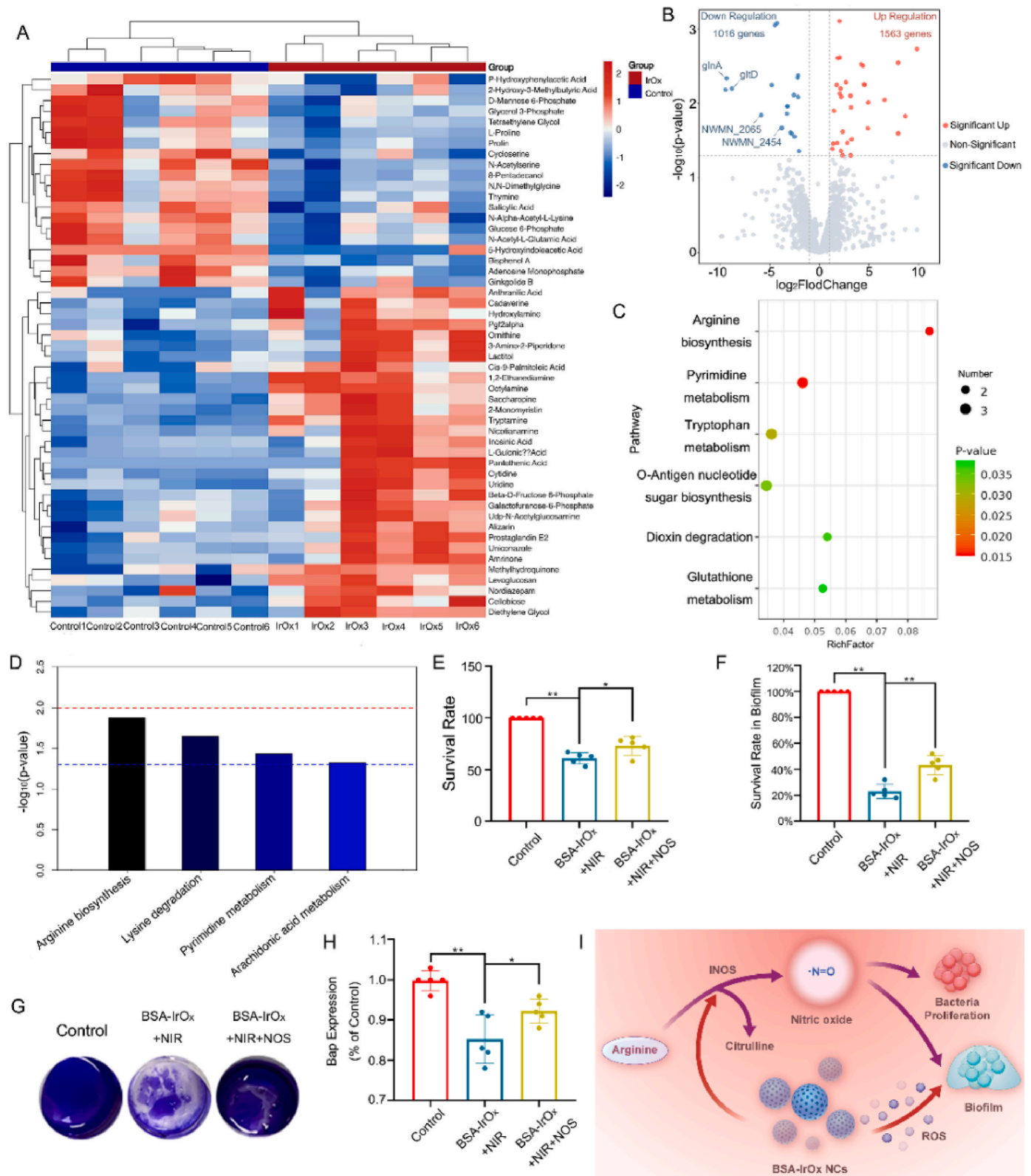
Fig. 3. BSA-IrO$_x$ NCs sterilize bacterial by altering the NOS of MRSA.
A. Heatmaps of metabolomics data from the control group and the BSA-IrO$_x$ + NIR group after 1 day of treatment. B. Volcano plots of transcriptomic data after 1 day of treatment in the control group and the BSA-IrO$_x$ + NIR group. C. Bubble map of the bacterial metabolomics KEGG analysis results between control and BSA-IrO$_x$ + NIR groups. D. KEGG pathway analysis of the combination the metabolomic and transcriptomic of control and BSA-IrO$_x$ + NIR groups. E. Survival rates of bacteria after different treatments, * represents $p < 0.05$ and ** represents $p < 0.01$, n = 5. F. Crystal violet analysis of bacterial biofilms after different treatments. G. Statistical analysis of the crystal violet staining after different treatments, ** represents $p < 0.01$, n = 5. H. ELISA results of the Bap of bacteria after different treatments, * represents $p < 0.05$ and ** represents $p < 0.01$, n = 5. I. Synergistic antibacterial mechanism of BSA-IrO$_x$ NCs + NIR through NOS pathway inhibition.

restored to a certain extent after the addition of NOS (Fig. S19), and fluorescence results also demonstrated the antagonistic effect of NOS on the treatment (Fig. 3G). Enzyme-Linked Immunosorbent Assay (ELISA) results revealed that the addition of NOS reduced the therapeutic effect of BSA-IrO$_x$ NCs + NIR on Bap, an important extracellular matrix protein secreted by MRSA that plays a key role in biofilm development [45] (Fig. 3H). These findings suggest that BSA-IrO$_x$ NCs inhibits biofilm formation by suppressing NOS activity in MRSA.

In summary, we verified the bactericidal and antibiofilm effects of BSA-IrO$_x$ NCs through a series of in vitro bacterial culture tests and biofilm detection assays. The combination of transcriptomic and metabolomic analyses of MRSA suggested that BSA-IrO$_x$ NCs restrain ROS resistance in bacteria through the NOS pathway. This inhibition of the NOS pathway reduces the formation of endogenous NO, which not only interferes with metabolism related to cell division but also reduces the level of Bap. A decrease in Bap affects biofilm stability, greatly reducing bacterial resistance to ROS [46]. The large amount of ROS produced by BSA-IrO$_x$ NCs collaborates with the reduction in endogenous NO, making sterilization more efficient and thorough. This synergistic bactericidal action is the optimal strategy by which BSA-IrO$_x$ NCs combat MRSA infections and reduce resistance, providing an advantage over traditional antibiotics (Fig. 3I). At the same time, the inhibition of NOS in MRSA is likely to be why BSA-IrO$_x$ NCs can enhance the

bactericidal effect of vancomycin, which needs to be explored in subsequent studies. This hypothesis suggests that the reduction of NO, which helps bacteria resist ROS, may make MRSA more susceptible to vancomycin when treated with BSA-IrO$_x$ NCs. By elucidating the molecular mechanisms underlying the antibacterial and antibiofilm effects of BSA-IrO$_x$ NCs, this study offers valuable insights into the development of novel strategies for treating antibiotic-resistant bacterial infections.

2.5. In vivo antibacterial effect of BSA-IrO$_x$ NCs under NIR irradiation

To explore the in vivo antibacterial effect of BSA-IrO$_x$ NCs + NIR, we established a rat model of MRSA infection (Fig. 4A) after confirming their in vitro efficacy. H&E staining of the main organs revealed no obvious toxicity of BSA-IrO$_x$ NCs (Fig. S20), demonstrating their biosafety in rats. At the same time, metabolites of BSA-IrO$_x$ NCs were detected. Certain levels of Ir^{3+} were found in the urine and feces of rats, indicating that BSA-IrO$_x$ NCs can be safely metabolized over a long period of time (Fig. S21). We also conducted CCK-8 detection, hemolysis detection, and apoptosis flow detection with Human skin fibroblasts (HSFs), and the experimental results fully demonstrated the excellent biosafety of BSA-IrO$_x$ NCs (Figs. S22, S23, S24). These results not only show that BSA-IrO$_x$ NCs are safe and non-toxic, but they can also be safely excreted after metabolism by organisms, which indicates
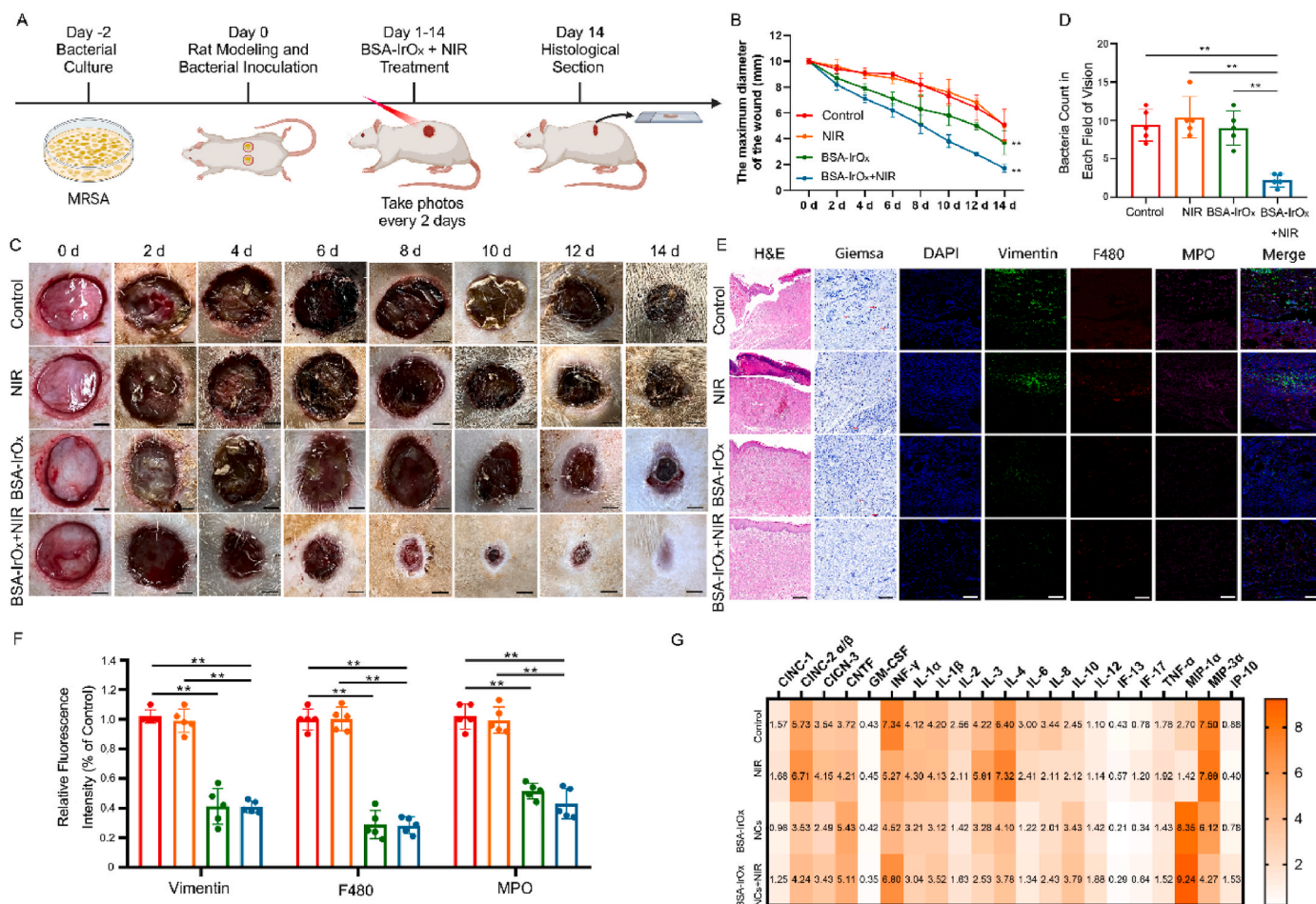

Fig. 4. Antibacterial effect of BSA-IrO$_x$ NCs + NIR in vivo.
A. Flow chart of the BSA-IrO$_x$ NCs + NIR antibacterial experiment in vivo. B. Representative images of infected wounds on rats over the course of treatment, scale bar: 250 μm. C. Changes in the diameter of infected wounds over time in rats, ** represents $p < 0.01$, n = 5. D. Representative H&E staining, Giemsa staining and immunofluorescence staining 14 days after the treatment of infected wounds in rats, scale bar: 100 μm for H&E and Masson staining, scale bar: 50 μm for immunofluorescence staining. E. Bacterial counts in Giemsa staining, ** represents $p < 0.01$, n = 5. F. Statistical analysis of three neutrophil markers in immunofluorescence staining, ** represents $p < 0.01$, n = 5. G. ELISA thermogram results of the inflammatory factor levels in tissues 14 days after the treatment of infected wounds in rats.

potential for clinical treatment. Additionally, we explored the temperature rise curve of BSA-IrO$_x$ NCs under 10 min of NIR irradiation, and the final temperature did not exceed 45 °C, indicating that BSA-IrO$_x$ NCs is not dangerous due to temperature rise (Fig. S25). We also include the

photothermal imaging results of in vivo experiments, showing that the temperature did not exceed 35 °C (Fig. S26), which indicates that the effect of PTT can be ignored in this study.

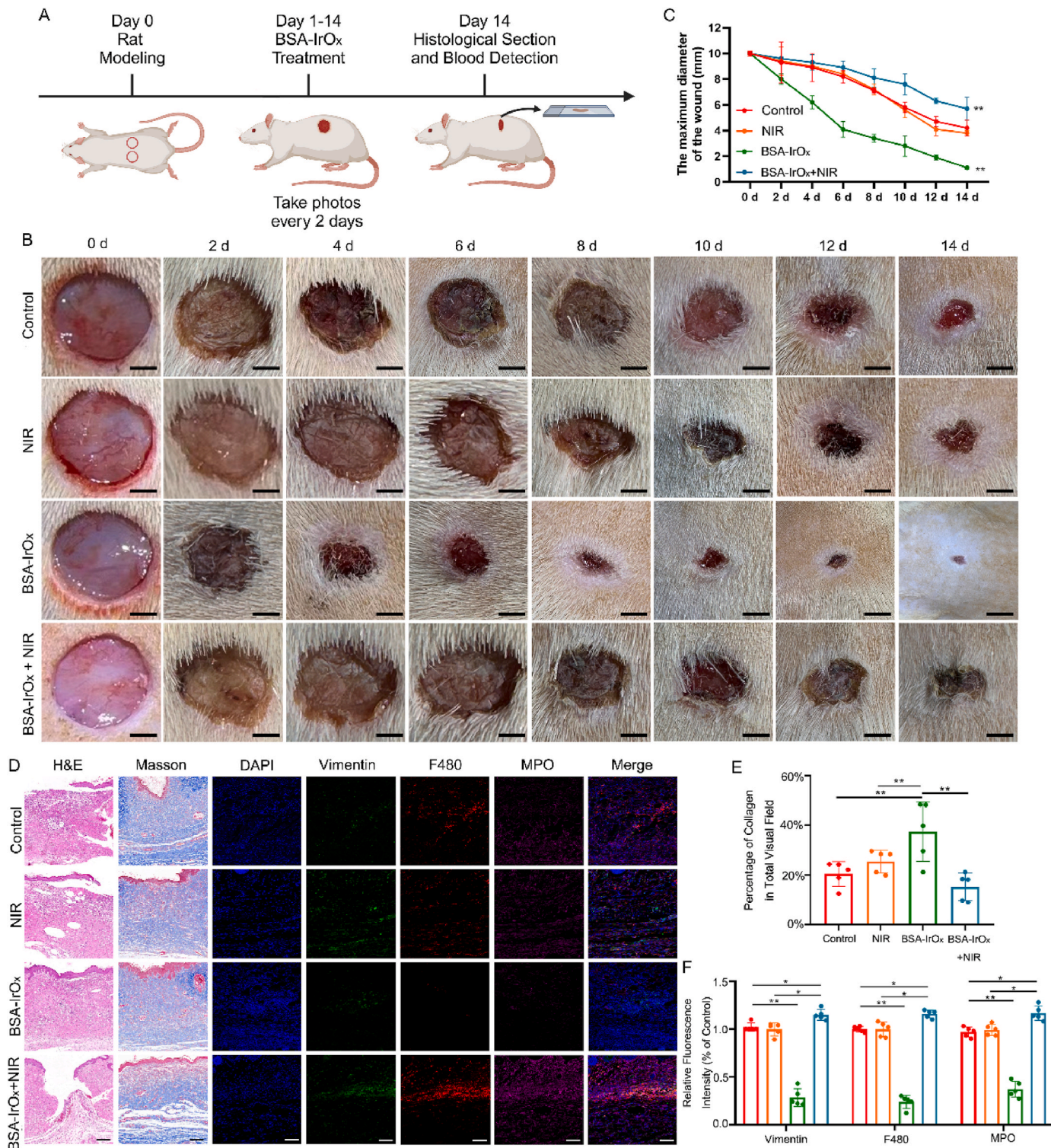In the control and NIR groups, infection caused purulent fluid

Fig. 5. BSA-IrO$_x$ NCs restore damaged skin wounds without NIR irradiation.
A. Flow chart of the BSA-IrO$_x$ NCs restoration experiment in vivo. B. Representative images of sterile wounds on rats over the course of treatment, scale bar: 250 μm. C. Changes in the sterile wound diameter with time in rats, ** represents p < 0.01, n = 5. D. Representative H&E staining, Masson staining and immunofluorescence staining 14 days after the treatment of sterile wounds in rats, scale bar: 100 μm for H&E and Masson staining, scale bar: 50 μm for immunofluorescence staining. E. Statistical analysis of the collagen in Masson staining, ** represents p < 0.01, n = 5. F. Statistical analysis of three neutrophil markers in immunofluorescence staining, * represents p < 0.05 and ** represents p < 0.01, n = 5.

buildup and severe skin tissue damage at the wound site, with persistent inflammatory reactions despite slight healing within 14 days. In contrast, BSA-IrO$_x$ NCs + NIR treatment suppressed the infection, with no purulent secretions observed (Fig. 4B). The healing time of wounds in the BSA-IrO$_x$ NCs + NIR group was 14 days, with a healing percentage of 89.8 %. These data are similar to clinical indicators for treating infected wounds, revealing the significant potential of BSA-IrO$_x$ NCs + NIR in wound infection treatment [47]. Moreover, the CAT-like and SOD activities of BSA-IrO$_x$ NCs reduced the inflammatory response at the wound site after withdrawing the NIR laser, leading to almost complete wound recovery within 14 days. Statistical analysis of wound size confirmed that BSA-IrO$_x$ NCs + NIR significantly reduced infected wound size on day 14 compared to the control treatment (Fig. 4C).

Skin tissue samples collected 14 days post-treatment were stained to assess the anti-infection and tissue repair effects of BSA-IrO$_x$ NCs + NIR (Fig. 4D). H&E staining revealed severe damage and purulent tissues in the control and NIR groups, while BSA-IrO$_x$ NCs + NIR treatment resulted in smooth tissue with no purulent areas. Giemsa staining showed numerous bacteria (red arrows) in the control, NIR, and BSA-IrO$_x$ groups, whereas the BSA-IrO$_x$ + NIR group had almost no bacteria (Fig. 4E). Immunofluorescence staining for vimentin, F480, and Myeloperoxidase (MPO) assessed neutrophil recruitment in the rat skin tissue. The control and NIR groups exhibited high neutrophil recruitment due to MRSA invasion, leading to inflammatory reactions. In contrast, the BSA-IrO$_x$ group had minimal neutrophil recruitment due to effective ROS scavenging, and the BSA-IrO$_x$ + NIR group also showed low neutrophil numbers due to infection treatment and ROS breakdown after stopping NIR irradiation. Fluorescence intensity analysis of the three neutrophil markers (Fig. 4F) confirmed that BSA-IrO$_x$ NCs reduced MRSA-induced neutrophil recruitment, thereby minimizing the subsequent inflammatory response. Three markers of neutrophils (Vimentin, F480, MPO) were detected, all of which are specific neutrophil proteins. The results showed a large number of neutrophilic infiltrations in the first two groups, indicating that the infection caused inflammatory cell infiltration and an inflammatory response [48]. After BSA-IrO$_x$ NCs + NIR treatment, the elimination of infection resulted in a significant reduction of inflammatory cells, which provided conditions for tissue repair. Notably, there was also less inflammatory cell infiltration in the pure BSA-IrO$_x$ NCs group due to the breakdown of ROS. We also tested the ROS content in the skin tissues of rats using the DPBF absorption value. The results showed that the ROS content in both the BSA group and the BSA-IrO$_x$ NCs + NIR group decreased to a certain extent, indicating that the ROS content in the tissues was reduced when the infection was suppressed (Fig. S27). ELISAs performed on tissues 14 days post-treatment (Fig. 4G) revealed that BSA-IrO$_x$ NCs reduced the expression of inflammatory factors such as IL-4, IL-6, and TNF-α, inhibiting the inflammatory response and reducing tissue damage.

2.6. BSA-IrO$_x$ NCs restore damaged skin wounds without NIR irradiation

To further verify the tissue repair ability of BSA-IrO$_x$ NCs in the absence of an NIR laser, we generated skin defects in rats without bacterial inoculation (Fig. 5A). After 14 days of treatment, the skin defects in the BSA-IrO$_x$ NCs-treated group recovered significantly, but the wounds expanded when an NIR laser was present, indicating that the ROS concentration changed with prolonged NIR laser exposure (Fig. 5B and C). Among them, the healing time of wounds in the BSA-IrO$_x$ group was 10 days, with a healing percentage of 94.6%. These results are similar to those observed in clinical wound treatments, highlighting the potential effectiveness of BSA-IrO$_x$ NCs in promoting rapid and efficient wound healing [49]. Skin tissue samples collected after 14 days of treatment were stained to observe the anti-infection and tissue repair effects of BSA-IrO$_x$ NCs + NIR (Fig. 5D). H&E staining revealed equally severe skin tissue damage in the control and NIR groups, which was significantly alleviated after BSA-IrO$_x$ NCs treatment. However, skin damage worsened under NIR laser irradiation, suggesting an increase in

ROS. Masson staining showed that BSA-IrO$_x$ NCs could repair damaged collagen fibers in tissues, strongly promoting skin regeneration (Fig. 5E).

Immunofluorescence staining of tissues revealed integral soft tissue repair with macrophage and fibroblast infiltration in the BSA-IrO$_x$ group, while the BSA-IrO$_x$ + NIR group exhibited obvious inflammation with extensive neutrophil infiltration (Fig. 5F). These results indicate that in the absence of an NIR laser, BSA-IrO$_x$ can repair tissue damage by reducing inflammation via the breakdown of ROS and a reduction in neutrophil infiltration. Under laser irradiation, BSA-IrO$_x$ will produce ROS due to PDT and aggravate tissue damage. In conclusion, the BSA-IrO$_x$ NCs treatment platform can switch between sterilization and tissue repair by regulating ROS, depending on the presence or absence of the NIR laser, enabling adequate treatment of infected wounds.

The extracellular matrix (ECM) represents a multifaceted and dynamic framework pivotal for cellular and tissue scaffolding. It intricately interacts with cells, orchestrating regulatory signals crucial for processes like cell migration, proliferation, differentiation, and apoptosis [50]. Throughout the phases of wound healing, ECM constituents undergo constant flux, playing pivotal roles in each stage. In this section, we delve into the pivotal role of the ECM within the inflammatory microenvironment [51,52]. Upon tissue injury, ECM components near the wound periphery emit distress signals, guiding immune cell infiltration. Additionally, the provisional matrix formed at the wound site acts as a scaffold, facilitating immune cell recruitment [53]. ECM scaffolds foster a conducive microenvironment, providing mechanical support for tissue repair and cellular regeneration [54]. Early in the inflammatory microenvironment, neutrophils detect damage signals and initiate an inflammatory cascade by generating H$_2$O$_2$ gradients via respiratory bursts. This process, coupled with the release of cytokines and chemokines from activated macrophages, T cells, endothelial cells, fibroblasts, and keratinocytes, further fuels the inflammatory response [55]. In our study, we observed that BSA-IrO$_x$ NCs effectively mitigate inflammatory cell infiltration and suppress the inflammatory response in wound healing in vivo. Subsequent in vitro experiments corroborated these findings, demonstrating that BSA-IrO$_x$ NCs attenuated the release of inflammatory mediators such as IL-1β, IL-6, and NOS by reducing ROS levels. Moreover, BSA-IrO$_x$ NCs increased the expression of intercellular compact linker proteins and adherent linker proteins, promoting ECM repair. These results indicate that BSA-IrO$_x$ NCs can control damage to the local inflammatory microenvironment through the decomposition of ROS, promoting the formation and destruction of the inflammatory microenvironment under NIR laser treatment.

2.7. Antibacterial and restorative effects of BSA-IrO$_x$ NCs in clinical human skin samples

To further elucidate the clinical therapeutic significance of BSA-IrO$_x$ NCs, we collected clinical skin samples to verify the efficacy of their bactericidal and restorative effects. A 3 mm diameter skin specimen was removed with a trephine and placed in complete culture medium for tissue culture (Fig. 6A). H&E staining performed on the human skin tissue after 3 days of treatment revealed significant wound repair (Fig. 6B and D). Statistical analysis of the wound width via H&E staining demonstrated the excellent tissue repair ability of BSA-IrO$_x$ NCs. To fully simulate severe clinical infection, MRSA was added to the human skin tissue culture, and samples were collected 3 days after treatment for SEM analysis (Fig. 6C and E). The electron microscopy results and bacterial counting showed that BSA-IrO$_x$ NCs + NIR PDT had excellent antibacterial efficacy. These results demonstrated the superior therapeutic effect of BSA-IrO$_x$ NCs in clinical samples compared to previous antibacterial nanomaterials [56–58]. To further measure the levels of inflammatory factors in sterile human skin tissue samples, we performed a qPCR assay to measure the mRNA levels of TNF-α and IL-1β in tissue homogenates (Fig. 6F and G). The results showed that BSA-IrO$_x$ NCs significantly reduced the levels of inflammatory factors in human skin tissue, indicating a substantial reduction in inflammation in clinical
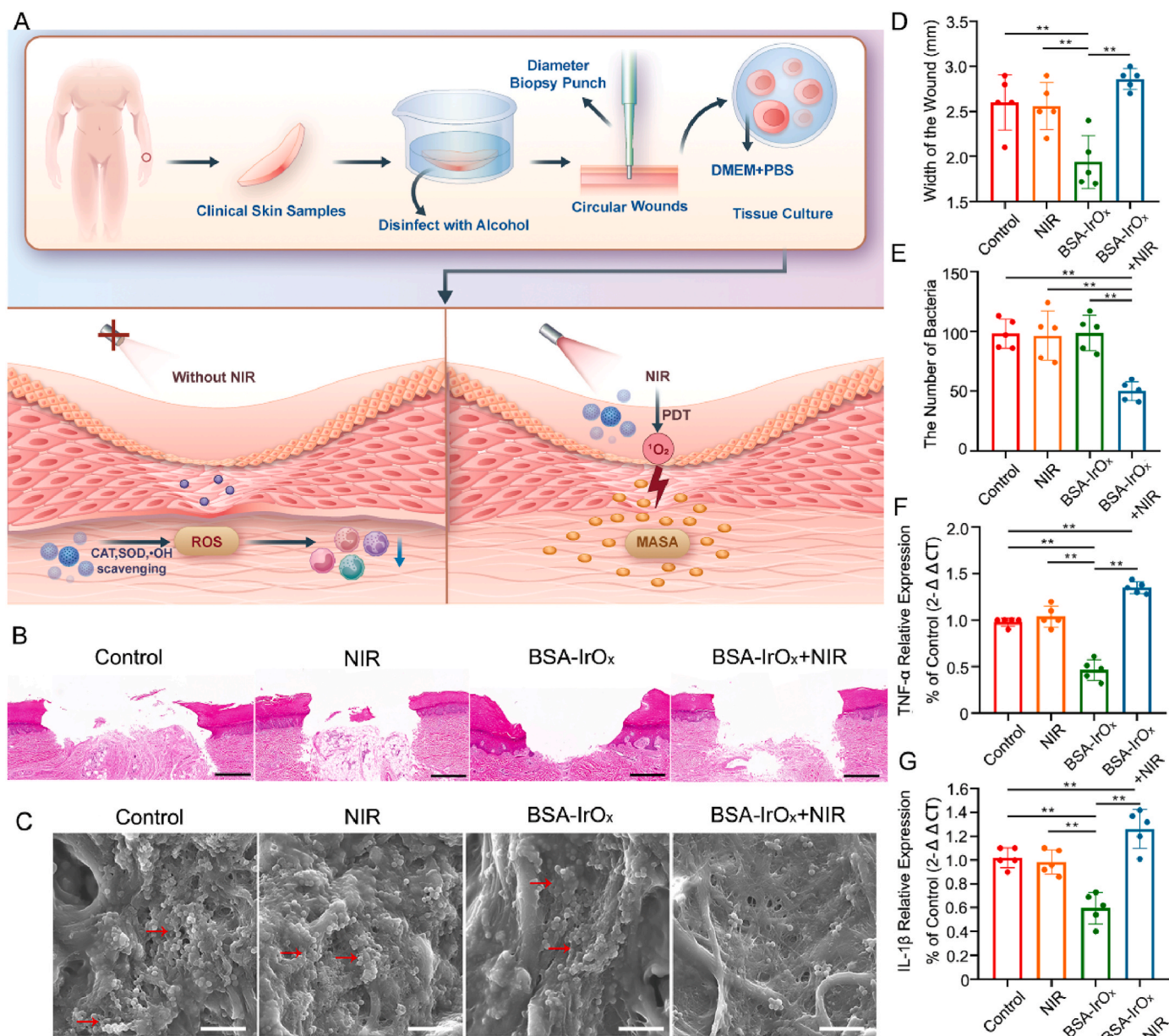
Fig. 6. Antibacterial and restorative effects of BSA-IrO$_x$ NCs in clinical human skin samples.
A. Fow chart of the antibacterial and restorative effects of BSA-IrO$_x$ NCs on clinical human skin specimens. B. Representative H&E staining results without NIR of sterile wounds, scale bar: 100 μm. C. Representative SEM images with NIR laser of infected wounds, scale bar: 1 μm. D. Statistical analysis of wounds width in H&E stained without NIR laser, ** represents $p < 0.01$, n = 5. E. Bacterial counts in SEM images with NIR, ** represents $p < 0.01$, n = 5. F. The qPCR results of the TNF-α level in human skin tissue samples, ** represents $p < 0.01$, n = 5. G. The qPCR results of the IL-1β level in human skin tissue samples, ** represents $p < 0.01$, n = 5.

samples. Based on the data collected from these clinical samples, we can conclude that the use of BSA-IrO$_x$ NCs has translational potential for addressing refractory infections in the clinic.

2.8. BSA-IrO$_x$ NCs inhibit fibroblast inflammation and increase cell junctions in vitro

We verified the tissue repair effects of BSA-IrO$_x$ NCs in vitro and explored the underlying molecular mechanisms. The scratch test showed that BSA-IrO$_x$ NCs significantly promoted fibroblast proliferation and wound repair (Fig. 7A and B). The migration test proved that BSA-IrO$_x$ NCs significantly enhanced fibroblast migration, accelerating skin healing (Fig. 7C and D). To further verify the inhibition of inflammation by BSA-IrO$_x$ NCs, HSFs were subjected to oxygen-glucose deprivation (OGD) to simulate injury and inflammation. Western blot analysis of

treated HSFs showed that BSA-IrO$_x$ NCs significantly inhibited OGD-induced inflammation and strongly reduced the expression of IL-6, IL-1β, NOS, and TNF-α (Fig. 7E and F). By reducing inflammatory factor levels, BSA-IrO$_x$ NCs can increase the expression of cell junction proteins. Immunofluorescence staining of fibroblasts revealed that BSA-IrO$_x$ NCs increased the expression of both tight and adherens junction proteins, demonstrating a significant positive impact on cell junctions (Fig. 7G and Fig. S28). These results provide mechanistic insights into the tissue repair effects of BSA-IrO$_x$ NCs, highlighting their potential for promoting wound healing and reducing inflammation in vitro.

Cell junctions, crucial components of the ECM, play vital roles in endothelial tissue repair [59]. These proteins are categorized into tight junction proteins and adherens junction proteins, both of which are essential for intercellular linking and tissue stability [60]. Inflammatory proteins such as matrix metalloproteinases (MMPs) can degrade and
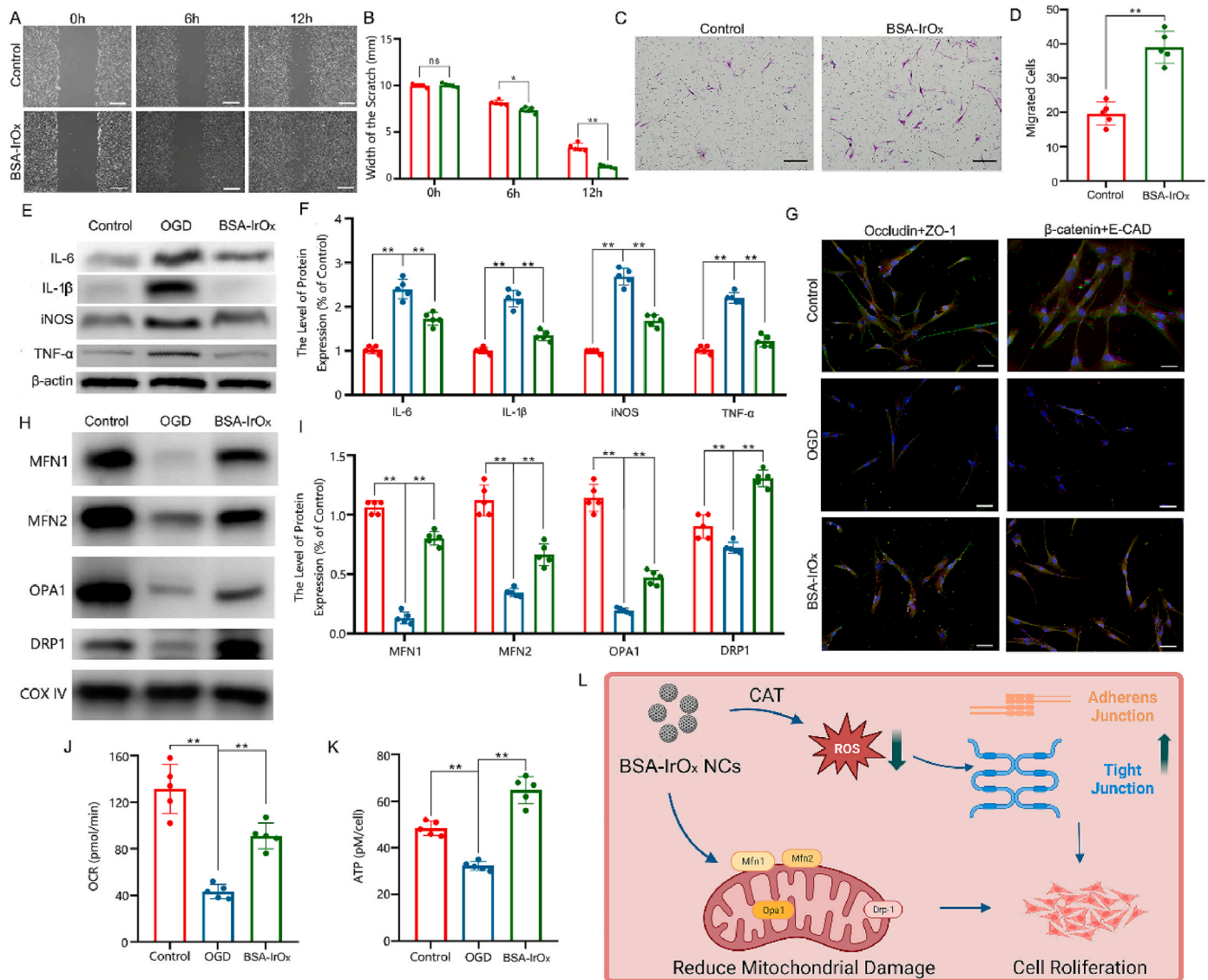
Fig. 7. BSA-IrO$_x$ NCs inhibit HSFs inflammation by enhancing the functions of the extracellular matrix and mitochondria in vitro.
A. Results of scratch tests on HSFs. B. Statistical analysis of scratch tests of HSFs, * represents p < 0.05 and ** represents p < 0.01, n = 5, scale bar: 500 μm. C. Results of migration tests on HSFs. Scale bar: 20 μm. D. Cell count of HSFs that migrated to subcompartments of the Transwell insert, ** represents p < 0.01, n = 5. E. Representative results of WB test of HSFs after different treatments. F. Statistical analysis of WB test of HSFs after different treatments, ** represents p < 0.01, n = 5. G. Representative immunofluorescence results of HSFs after different treatments, scale bar: 10 μm. H. Representative results of WB test of HSFs after different treatments. I. Statistical analysis of WB test of HSFs after different treatments. ** represents p < 0.01, n = 5. J. Results of OCRs test of HSFs, ** represents p < 0.01, n = 5. K. Results of ATP level of HSFs, ** represents p < 0.01, n = 5. L. L. Synergistic tissue restoration mechanism of BSA-IrO$_x$ NCs without NIR by increasing cell junctions and repairing mitochondrial function.

reduce cell junction proteins when secreted in large quantities [61]. However, when inflammation is suppressed, MMPs activity decreases, leading to increased cell junction protein expression and promoting tissue restoration [62]. The reduction in inflammation also stimulates fibroblast proliferation, and the resulting increase in intercellular links further accelerates the process of restoration at the tissue level [63]. In summary, BSA-IrO$_x$ NCs inhibit the secretion of inflammatory factors by decomposing ROS, promoting the expression of cell junction proteins, and reducing the inflammatory microenvironment, thereby fostering tissue repair. These findings highlight the multifaceted approach of BSA-IrO$_x$ NCs in promoting wound healing by targeting key cellular and molecular mechanisms involved in the restoration process.

2.9. BSA-IrO$_x$ NCs promote restoration by reducing mitochondrial damage

ROS outbursts are the primary cause of mitochondrial damage. Mitochondria, the functional units of cells, play crucial roles in cell metabolism. Many studies have shown that mitochondrial damage is related to inflammation and ferroptosis, making it an important molecular mechanism. As BSA-IrO$_x$ NCs can eliminate ROS and inhibit inflammation, we examined the mitochondrial function of treated fibroblasts. Western blot experiments revealed that BSA-IrO$_x$ NCs significantly increased the expression of Mitofusin 1 (MFN1), MFN2, Optic Atrophy 1 (OPA1), and Dynamin-relatedprotein 1 (DRP1) (Fig. 7H and I). MFN1 and MFN2 are proteins in the mitochondrial outer membrane that stabilize mitochondria and play essential roles in mitochondrial division [64]. OPA1, a protein in the inner mitochondrial membrane, is critical for mitochondrial division. DRP1 is related to mitochondrial

function and can alleviate mitochondrial damage to a certain extent [65]. Therefore, the Western blot results demonstrated that BSA-IrO$_x$ NCs can reduce mitochondrial damage by regulating related proteins. Furthermore, we explored the effects of BSA-IrO$_x$ NCs on mitochondrial function by measuring the OCR (Fig. 7J) and ATP content (Fig. 7K). BSA-IrO$_x$ NCs significantly increased the OCR and ATP content of fibroblasts, suggesting that mitochondrial function was restored. These findings highlight the potential of BSA-IrO$_x$ NCs in preserving mitochondrial integrity and function, which may contribute to their anti-inflammatory and tissue repair properties.

Injury can cause an increase in ROS, which promotes the secretion of inflammatory factors and leads to the formation of an inflammatory microenvironment. In this microenvironment, both cell junctions and mitochondrial function are significantly affected [66]. Mitochondria are particularly vulnerable to high levels of ROS, which activate molecular pathways associated with ferroptosis, further aggravating mitochondrial damage [67,68]. Consequently, mitochondrial damage leads to decreased aerobic respiration and reduced cell function, exacerbating tissue damage and delaying repair processes [69,70]. Therefore, it is crucial to repair mitochondrial damage and enhance mitochondrial function while simultaneously reducing inflammation. Only when mitochondrial function is restored can cells have sufficient energy to participate in tissue repair. Our study demonstrated that BSA-IrO$_x$ NCs can increase cell junctions and restore mitochondrial function through ROS scavenging, thereby significantly promoting tissue regeneration (Fig. 7L). These findings emphasize the importance of targeting multiple cellular processes, such as inflammation, cell junctions, and mitochondrial function, to optimize tissue repair strategies. By addressing these key aspects, BSA-IrO$_x$ NCs offer a promising approach for enhancing wound healing and tissue regeneration.

3. Conclusions

In this study, we developed bovine serum albumin-iridium oxide nanoclusters (BSA-IrO$_x$ NCs) for the treatment of infected wounds using a photo-regulated ROS strategy. The designed BSA-IrO$_x$ NCs not only inhibited bacterial activity under 808 nm laser irradiation but also mimicked antioxidant enzyme-like activities to eliminate ROS. By reducing the secretion of inflammatory factors and increasing mitochondrial function, BSA-IrO$_x$ NCs restored impaired skin in the absence of NIR laser irradiation. This work demonstrated that IrO$_x$-based nanozymes can effectively regulate ROS levels by switching the NIR laser on and off. We believe this study has provided a novel photo-regulating strategy with an innovative design rationale and biological mechanism, illustrating its potential use for infected wound healing therapy. The ability to control ROS levels using an external stimulus, such as NIR light, offers a promising approach for managing the complex interplay between inflammation, bacterial infection, and tissue repair in the context of wound healing. The development of BSA-IrO$_x$ NCs represents a significant step forward in the field of nanomedicine, highlighting the importance of multifunctional nanomaterials that can address multiple aspects of the wound healing process simultaneously.

The limitation of this study is that more clinical sample experiments were not conducted to determine various parameters of BSA-IrO$_x$ NCs used in clinical treatment, including concentration, duration of action, and NIR-related parameters. These aspects need to be explored in further studies. Additionally, the final metabolites of BSA-IrO$_x$ NCs still need to be further clarified to ensure complete understanding of its metabolic pathways and safety profile in clinical applications. Further research and clinical translation of this technology could lead to improved outcomes for patients suffering from infected wounds and other related conditions.

4. Experimental section

Clinical samples: Skin samples were collected from patients who

underwent surgery at Shanghai Sixth People's Hospital. After receiving patients' written informed consent and approval from Shanghai Sixth People's Hospital's Ethics Committee in compliance with current laws and institutional guidelines, only the remaining clinically healthy skin that was not required for diagnostic purposes was examined. The approval number was 2022-KY-139 (K).

In vitro antibacterial effect of BSA-IrO$_x$ NCs: Staphylococcus aureus (biofilm-positive, American Type Culture Collection (ATCC) 43300) was used in our investigation to assess the antibacterial capabilities of the BSA-IrO$_x$ NCs. In new Tryptic Soy Broth (TSB) culture medium, the strains were grown to 10^9/mL at 37 °C for an entire night. The evaluation of the antibiofilm effects of the nanomaterials was conducted in five experimental groups using the MRSA biofilms that formed on poly(ether-ether-ketone) (PEEK) discs: control group, NIR group (808 nm, 4.0 W/cm^2, 5 min), BSA-IrO$_x$ group (1.6 mg/mL, 500 μL), and BSA-IrO$_x$ group (1.6 mg/mL, 500 μL) + NIR laser group (808 nm, 4.0 W/cm^2, 5 min). All of the samples were rinsed three times after treatment in preparation for the ensuing studies.

For SEM, all of the samples were fixed overnight at 4 °C in 2.5 % glutaraldehyde. After that, they were dehydrated using ethanol at progressively higher concentrations (30 %, 50 %, 70 %, 80 %, 95 %, 100 %). Following freeze-drying and gold spraying, the samples were examined using a field emission scanning electron microscope (JSM-7800F, JEOL, Japan). Using a biology TEM, the treated bacteria's morphology was examined. After being centrifuged and fixed for 3 h with 2.5 % glutaraldehyde, the treated bacteria were Phosphate Buffered Saline (PBS)-washed three times. The bacteria were then fixed once more for 2 h at room temperature using 1 % aqueous OsO4. After three PBS washes, the samples were dehydrated using ethanol solutions (30 %, 50 %, 70 %, 80 %, 90 %, and 100 %) for a duration of 15 min. Subsequently, the samples were infused with medium. The samples were subsequently imbedded for 48 h at 60 °C, sliced into 60-nm-thick sheets using a Leica UC7 microtome fitted with a Tecnai G2 20 TWIN diamond knife, and dyed with uranyl acetate. Lastly, TEM was used to view the structural portion of the bacterium. For the ROS assay, biofilms were incubated with a DCFH-DA diluent (10 mmol/L) at 37 °C for 20 min. Excess dye was then removed, and the samples were rinsed three times with PBS for subsequent observation using confocal laser scanning microscopy (CLSM). For CLSM, adhesive bacteria on titanium plates from each group were placed into a new 24-well plate, washed with fresh PBS, stained with a mixed dye (LIVE/DEAD BacLight Bacteria Viability Kit, Invitrogen) for 30 min, and photographed using CLSM. Viable microorganisms were stained green, while dead ones were stained red. For the crystal violet assay, bacteria were inoculated onto cell culture plates, each containing about 10^4 bacteria, and then cultured at 37 °C for 24–48 h until a mature biofilm formed. Next, a medium containing the appropriate concentration of the tested compound was added, and the cell culture plate was placed in an incubator for the appropriate time. Finally, floating bacteria were removed by rinsing with methanol, and crystal violet was added for staining. Excess dye was removed by rinsing with methanol, and the crystal violet was dissolved by adding 33 % glacial acetic acid. The optical density value of each well was measured at 590 nm using an enzyme labeler.

Construction of a rat skin model of wounds: The animal surgeries for this study were approved by the Animal Care and Experiment Committee of the Shanghai Jiao Tong University Affiliated Sixth People's Hospital (ethical number: 2021-0380). Forty SD rats (8 weeks) were randomly divided into 4 groups (control, NIR, BSA-IrO$_x$ and BSA-IrO$_x$ + NIR). In our experiments, these rats were first anesthetized by intraperitoneal injection of 0.3 % pentobarbital sodium. Subsequently, the hair on the back was shaved, and the area was scrubbed with medicinal alcohol twice. Next, a sterile metal trephine (1 cm in diameter) was used to drill two symmetrical circular wounds on the back skin of the rats. Then, in the infected wound experiment, the wound was inoculated with 200 μL of 10^9 MRSA cells. In the sterile wound experiment, 200 μL of normal saline was used instead. In the control group, no

treatment was given to the rats. In the NIR group, 10 min of infrared irradiation at 808 nm and 1.0 W/cm^2 was performed daily. In the BSA-IrO_x group, 4.8 mg/mL of 500 μL nanomaterial was added after the addition of bacteria, and then no infrared irradiation was applied. In the BSA-IrO_x + NIR group, the rats were irradiated for 10 min every day after the nanomaterials were added. Photographs and wound cleaning were taken every day after the mold was made until samples were collected after 14 days.

Ex vivo human skin model of wound infection: Following the removal of adipose tissue, skin samples underwent thorough cleansing with a solution consisting of 3 parts Antibiotics, Antimycotics, and Antifungals (ABAM) followed by rinsing with PBS. Circular wounds were then meticulously created using biopsy punch tools with a diameter of 3 mm, while the wound and surrounding tissue rim were excised using 8 mm punch tools. Subsequently, the skin explants underwent a dual wash with DMEM supplemented with 10% FBS to ensure optimal culture conditions. Each skin explant was then individually cultured in 1 ml of culture medium, maintaining the epithelium at the air-liquid interface. The culture medium used was DMEM supplemented with 10% FBS. MRSA was incubated at 37 °C in TSB at a concentration of 10 CFU/ml. The skin wounds were then inoculated with either 10 μl of bacterial inoculum (10,000 CFUs) or various nanodrugs. The skin explants were cultured for 48 h, and the medium was changed every 12 h to facilitate biofilm formation and to select for adherent bacteria. After 48 h, the skin wounds were collected for analysis. The clean sterile skin tissue was stained with H&E to identify its morphological changes and healing. Infected skin tissue with bacteria was scanned by SEM to observe the surface morphology of clinical skin samples and to carry out bacteria counts to determine the infection situation.

Culture and detection of human fibroblasts: Human fibroblast CRL-2522 cells from the ATCC were cultured in high-glucose DMEM supplemented with 10 % fetal bovine serum and placed in a 5 % CO_2 incubator at 37 °C. The migration ability of the CRL-2522 cells was measured with a Corning Transwell chamber (8 μm aperture). The experimental steps were as follows: cells in the logarithmic growth stage were removed, the cells were suspended in culture medium containing 1 % FBS, and the cells were inoculated into the chamber at a density of 2 $\times 10^4$ cells/well in a 200 μL system. In addition, 500 μL of 1 % FBS-DMEM containing different stimulus factors was added to a 24-well plate. The cells were prepared with 100 μL of PBS and BSA-IrO_x NCs, and then the cells were gently placed in a pore plate and incubated in a 5 % CO_2 incubator at 37 °C for 10 h. The cells were removed after incubation, and the cells on the bottom and upper layers of the cells that did not migrate were gently removed with cotton swabs. The cells were washed twice with PBS and fixed in 4 % paraformaldehyde for 20 min. The cells that migrated to the lower part of the chamber were observed under an inverted microscope. Five fields were randomly selected for imaging, and the number of cells was counted. The average values of the results were recorded. The experiment was repeated 5 times.

OGD and reperfusion treatment: To mimic skin damage in vitro, HSFs underwent OGD followed by reperfusion treatment. Initially, the culture medium was aspirated, and the cells were gently washed three times with PBS to eliminate residual glucose. Subsequently, the cells were exposed to glucose-free DMEM within a hypoxic incubator (oxygen concentration ≤ 1 %) for 3 h to induce hypoxic injury, thereby simulating conditions akin to in vivo skin damage. After the OGD exposure period, the cells were restored to standard culture conditions. Glucose-containing DMEM was reintroduced, and the oxygen concentration was set to 20 %, maintaining the cells under normal culture conditions for 24 h. As a control measure, a subset of cells underwent a different protocol. These cells were washed three times with DMEM containing glucose and then cultured in glucose-containing DMEM under normoxic conditions with an oxygen concentration of 20 %.

Extraction of mitochondrial protein from HSFs: Three milliliters of precooled HSFs was removed for washing, and 1 mL of precooled HSF was added to each 10 cm Petri dish. The cells were scraped off and then transferred to a 15 mL centrifuge tube with a total volume of approximately 2 mL. The cells were centrifuged at 700g for 5 min in a precooled centrifuge at 4 °C. The supernatant was discarded, and the cells were crushed under high pressure (2000 psi on ice for 10 min). The broken cell products were then transferred to a centrifuge tube using a 1 mL pipette and centrifuged at 700g for 8 min in a precooled centrifuge at 4 °C. The supernatant was carefully removed to a new centrifuge, and placed on ice. After the 500 μL suspension, the precipitate was centrifuged at 700g for 5 min on a precooled centrifuge at 4 °C. The supernatant was carefully removed and mixed with S1, with a total volume of approximately 3 mL. The samples were centrifuged at 17000 g in a precooled centrifuge at 4 °C for 11 min. The supernatant was carefully removed, which contained cytoplasmic protein, and the precipitate was collected from the mitochondria. The Baize precipitate was carefully added to a new centrifuge tube, and 50 μL of PBS was added for resuspension. The extracted mitochondria were stored at −80 °C, and the protein concentration was detected by the Bradford method after proper mitochondrial cleavage.

Statistical analysis: In vitro experiments were repeated at least three times, and in vivo experiments were repeated at least six times. All the data are presented as the mean and standard deviation. GraphPad Prism v9.0.0 (La Jolla, CA, USA) was used for statistical analysis. Statistical significance was calculated using one-way Analysis of Variance (ANOVA) and Student's *t*-test and is denoted as * ($p < 0.05$) or ** ($p < 0.01$).

Funding

Ethics approval and consent to participate

Clinical samples: Skin samples were collected from patients who underwent surgery at Shanghai Sixth People's Hospital. Only the remaining clinically healthy skin that was not needed for diagnostic purposes was analyzed after obtaining written informed consent from the patients and approval from the Ethics Committee of Shanghai Sixth People's Hospital in accordance with current regulations and institutional guidelines. The approval number was 2022-KY-139 (K).

All animal experiments conformed to the Guide for the Care and Use of Laboratory Animals from the National Institutes of Health, and all procedures were approved by the Animal Research Committee of the Sixth People's Hospital at Shanghai Jiao Tong University.

CRediT authorship contribution statement

Xin Wang: Writing – review & editing, Writing – original draft, Investigation, Conceptualization. **Jianing Ding:** Writing – original draft, Validation. **Xiao Chen:** Writing – review & editing, Validation, Investigation. **Sicheng Wang:** Investigation. **Zhiheng Chen:** Validation, Data curation. **Yuanyuan Chen:** Methodology, Investigation. **Guowang Zhang:** Validation, Supervision. **Ji Liu:** Resources, Methodology. **Tingwang Shi:** Validation, Supervision. **Jian Song:** Writing – review & editing. **Shihao Sheng:** Writing – review & editing. **Guangchao Wang:** Writing – review & editing. **Jianguang Xu:** Writing – original draft. **Jiacan Su:** Investigation, Conceptualization. **Wei Zhang:** Validation, Investigation. **Xiaofeng Lian:** Writing – review & editing, Writing – original draft, Investigation, Funding acquisition, Data curation, Conceptualization.

Declaration of competing interest

The authors declare that they have no known competing financial interests or personal relationships that could have appeared to influence the work reported in this paper.

Appendix A. Supplementary data

Supplementary data to this article can be found online at https://doi.org/10.1016/j.bioactmat.2024.07.009.

References

[1] J.L. Seidelman, C.R. Mantyh, D.J. Anderson, Surgical site infection prevention: a review, JAMA 3 (2023) 244–252.

[2] G. Guo, Z. Liu, J. Yu, Y. You, M. Li, B. Wang, J. Tang, P. Han, J. Wu, H. Shen, Neutrophil function conversion driven by immune switchpoint regulator against diabetes-related biofilm infections, Advanced materials 8 (2024) 2310320.

[3] R.A.G. da Silva, J.J. Wong, H. Antypas, P.Y. Choo, K. Goh, S. Jolly, C. Liang, L. Tay Kwan Sing, M. Veleba, G. Hu, J. Chen, K.A. Kline, Mitoxantrone targets both host and bacteria to overcome vancomycin resistance in Enterococcus faecalis, Sci. Adv. 8 (2023) 9280.

[4] P.R. Guda, A. Sharma, A.J. Anthony, M.S. ElMasry, A.D. Couse, P.D. Ghatak, A. Das, L. Timsina, J.C. Trinidad, S. Roy, D.E. Clemmer, C.K. Sen, S. Ghatak, Nanoscopic and functional characterization of keratinocyte-originating exosomes in the wound fluid of non-diabetic and diabetic chronic wound patients, Nano Today 52 (2023) 101954.

[5] A. Frei, A.D. Verderosa, A.G. Elliott, J. Zuegg, M.A.T. Blaskovich, Metals to combat antimicrobial resistance, Nat. Rev. Chem 3 (2023) 202–224.

[6] M. Chang, T.T. Nguyen, Strategy for treatment of infected diabetic foot ulcers, Accounts of chemical research 5 (2021) 1080–1093.

[7] S. Li, X. Wang, Z. Yan, T. Wang, Z. Chen, H. Song, Y. Zheng, Microneedle patches with antimicrobial and immunomodulating properties for infected wound healing, Adv. Sci. 10 (2023) 2300576.

[8] C. Xu, K. Pu, Second near-infrared photothermal materials for combinational nanotheranostics, Chem. Soc. Rev. 50 (2021) 1111–1137.

[9] W. Fan, P. Huang, X. Chen, Overcoming the Achilles' heel of photodynamic therapy, Chem. Soc. Rev. 45 (2016) 6488–6519.

[10] J. Zhang, Q. Jia, Z. Yue, J. Huo, J. Chai, L. Yu, R. Nie, H. Shao, Y. Zhao, P. Li, W. Huang, An electroluminodynamic flexible device for highly efficient eradication of drug-resistant bacteria, Advanced materials 34 (2022) 2200334.

[11] J. Gao, Y. Yan, S. Gao, H. Li, X. Lin, J. Cheng, Y. Hu, K. Cai, X. Zhang, J. Li, Heterogeneous Cu2O-SnO2 doped polydopamine fenton-like nanoenzymes for synergetic photothermal-chemodynamic antibacterial application, Acta Biomater. 173 (2022) 420–431.

[12] X. Qiao, J. Liang, L. Qiu, W. Feng, G. Cheng, Y. Chen, H. Ding, Ultrasound-activated nanosonosensitizer for oxygen/sulfate dual-radical nanotherapy, Biomaterials 301 (2023) 122252.

[13] R. Chen, S. Huang, T. Lin, H. Ma, W. Shan, F. Duan, J. Lv, J. Zhang, L. Ren, L. Nie, Photoacoustic molecular imaging-escorted adipose photodynamic-browning synergy for fighting obesity with virus-like complexes, Nat. Nanotechnol. 16 (2021) 455–465.

[14] K. Cheng, H. Wang, S. Sun, M. Wu, H. Shen, K. Chen, Z. Zhang, S. Li, H. Lin, Specific chemiluminescence imaging and enhanced photodynamic therapy of bacterial infections by hemin-modified carbon dots, Small 19 (2023) 2207868.

[15] A. Maleki, J. He, S. Bochani, V. Nosrati, M.A. Shahbazi, B. Guo, Multifunctional photoactive hydrogels for wound healing acceleration, ACS Nano 15 (2021) 18895–18930.

[16] C.G. Weindel, E.L. Martinez, X. Zhao, C.J. Mabry, S.L. Bell, K.J. Vail, A.K. Coleman, J.J. VanPortfliet, B. Zhao, A.R. Wagner, H.M. Scott, P. Li, A.P. West, J. Karpac, K.L. Patrick, R.O. Watson, Mitochondrial ROS promotes susceptibility to infection via gasdermin D-mediated necroptosis, Cell 185 (2022) 3214–3231.

[17] C. Holze, C. Michaudel, C. Mackowiak, D.A. Haas, C. Benda, P. Hubel, F. L. Pennemann, D. Schnepf, J. Wettmarshausen, M. Braun, D.W. Leung, G. K. Amarasinghe, F. Perocchi, P. Staeheli, B. Ryffel, A. Pichlmair, Oxeiptosis, a ROS-induced caspase-independent apoptosis-like cell-death pathway, Nat. Immunol. 19 (2018) 130–140.

[18] X. Qi, E. Cai, Y. Xiang, C. Zhang, X. Ge, J. Wang, Y. Lan, H. Xu, R. Hu, J. Shen, An immunomodulatory hydrogel by hyperthermia-assisted self-cascade glucose depletion and ROS scavenging for diabetic foot ulcer wound therapeutics, Advanced materials 35 (2023) 2306632.

[19] S. Willenborg, D.E. Sanin, A. Jais, X. Ding, T. Ulas, J. Nüchel, M. Popović, T. MacVicar, T. Langer, J.L. Schultze, A. Gerbaulet, A. Roers, E.J. Pearce, J. C. Brüning, A. Trifunovic, S.A. Eming, Mitochondrial metabolism coordinates stage-specific repair processes in macrophages during wound healing, Cell Metabol. 33 (12) (2021) 2398–2414.

[20] P. Patil, K.A. Russo, J.T. McCune, A.C. Pollins, M.A. Cottam, B.R. Dollinger, C. R. DeJulius, M.K. Gupta, R. D'Arcy, J.M. Colazo, F. Yu, M.G. Bezold, J.R. Martin, N. L. Cardwell, J.M. Davidson, C.M. Thompson, A. Barbul, A.H. Hasty, S.A. Guelcher, C.L. Duvall, Reactive oxygen species-degradable polythioketal urethane foam dressings to promote porcine skin wound repair, Sci. Transl. Med. 14 (2022) 6586.

[21] S. Qiu, X. Zhong, X. Meng, S. Li, X. Qian, H. Lu, J. Cai, Y. Zhang, M. Wang, Z. Ye, H. Zhang, P. Gao, Mitochondria-localized cGAS suppresses ferroptosis to promote cancer progression, Cell Res. 33 (2023) 299–311.

[22] W. Yitong, Y. Ting, L. Jinxiu, X. Yafeng, W. Ruiqi, K. Qinfei, G.S. Steve, X. He, L. Kaili, Hierarchical micro/nanofibrous scaffolds incorporated with curcumin and zinc ion eutectic metal organic frameworks for enhanced diabetic wound healing via anti-oxidant and anti-inflammatory activities, Chem. Eng. J. 402 (2020) 126273.

[23] Y. Zhuang, S. Jiang, X. Deng, A. Lao, X. Hua, Y. Xie, L. Jiang, X. Wang, K. Lin, Energy metabolism as therapeutic target for aged wound repair by engineered extracellular vesicle, Sci. Adv. 15 (2024) l0372.

[24] Y. Yao, X. Lei, Y. Wang, G. Zhang, H. Huang, Y. Zhao, S. Shi, Y. Gao, X. Cai, S. Gao, Y. Lin, A mitochondrial nanoguard modulates redox homeostasis and bioenergy metabolism in diabetic peripheral neuropathy, ACS Nano 17 (2023) 22334–22354.

[25] X. Xia, H. Li, X. Xu, G. Zhao, M. Du, Facilitating pro-survival mitophagy for alleviating Parkinson's disease via sequence-targeted Lycopene Nanodots, ACS Nano 17 (2023) 17979–17995.

[26] M.B. Dickerson, K.H. Sandhage, R.R. Naik, Protein- and peptide-directed syntheses of inorganic materials, Chemical reviews 11 (2008) 4935–4978.

[27] S. Fu, H. Chen, W. Yang, X. Xia, S. Zhao, X. Xu, P. Ai, Q. Cai, X. Li, Y. Wang, J. Zhu, B. Zhang, J.C. Zheng, ROS-targeted depression therapy via BSA-incubated ceria nanoclusters, Nano Lett. 11 (2022) 4519–4527.

[28] H. Yuan, F. Li, L. Jia, J. Guo, T. Kong, T. Meng, Bacteria-inspired aqueous-in-aqueous compartmentalization by in situ interfacial biomineralization, Small Methods 2 (2023) e2201309.

[29] T. Nie, W. Zou, Z. Meng, L. Wang, T. Ying, X. Cai, J. Wu, Y. Zheng, B. Hu, Bioactive iridium nanoclusters with glutathione depletion ability for enhanced sonodynamic-triggered ferroptosis-like cancer cell death, Advanced materials 34 (2022) 2206286.

[30] W. Du, J. Wang, L. Zhou, J. Zhou, L. Feng, C. Dou, Q. Zhang, X. Zhang, Q. Zhao, X. Cai, J. Wu, Y. Zheng, Y. Li, Transferrin-targeted iridium nanoagglomerates with multi-enzyme activities for cerebral ischemia-reperfusion injury therapy, Acta Biomater. 166 (2023) 524–535.

[31] L. Huang, T. Nie, L. Jiang, Y. Chen, Y. Zhou, X. Cai, Y. Zheng, L. Wang, J. Wu, T. Ying, Acidity-biodegradable iridium-coordinated nanosheets for amplified ferroptotic cell death through multiple regulatory pathways, Adv. Healthcare Mater. 12 (2023) 2202562.

[32] W. Zhen, Y. Liu, L. Lin, J. Bai, X. Jia, H. Tian, X. Jiang, BSA-IrO2: catalase-like nanoparticles with high photothermal conversion efficiency and a high X-ray absorption coefficient for anti-inflammation and antitumor theranostics, Angew. Chem. 32 (2018) 10309–10313.

[33] Vijay S. Adusumilli, Tara L. Walker, Rupert W. Overall, Gesa M. Klatt, Salma A. Zeidan, Sara Zocher, Dilyana G. Kirova, Konstantinos Ntitsias, Tim J. Fischer, Alex M. Sykes, Susanne Reinhardt, Andreas Dahl, Jörg Mansfeld, Annette E. Rünker, Gerd Kempermann, ROS dynamics delineate functional states of hippocampal neural stem cells and link to their activity-dependent exit from quiescence, Cell Stem Cell 2 (2021) 300–314.

[34] P. Sun, K. Li, X. Liu, J. Wang, X. Qiu, W. Wei, J. Zhao, Peptide-mediated aqueous synthesis of NIR-II emitting Ag2S quantum dots for rapid photocatalytic bacteria disinfection, Angew. Chem. 14 (2023) 202300085.

[35] Y. Wang, X. Shen, S. Ma, Q. Guo, W. Zhang, L. Cheng, L. Ding, Z. Xu, J. Jiang, L. Gao, Oral biofilm elimination by combining iron-based nanozymes and hydrogen peroxide-producing bacteria, Biomater. Sci. 8 (2020) 2447–2458.

[36] J. Ding, X. Wang, W. Liu, C. Ding, J. Wu, R. He, X. Zhang, Biofilm microenvironment activated antibiotic adjuvant for implant-associated infections by systematic iron metabolism interference, Adv. Sci. 2 (2024) 2400862.

[37] Z. Liu, K. Guo, L. Yan, K. Zhang, Y. Wang, X. Ding, N. Zhao, F.J. Xu, Janus nanoparticles targeting extracellular polymeric substance achieve flexible elimination of drug-resistant biofilms, Nat. Commun. 14 (2023) 5132.

[38] A. Zhang, H. Wu, X. Chen, Z. Chen, Y. Pan, W. Qu, H. Hao, D. Chen, S. Xie, Targeting and arginine-driven synergizing photodynamic therapy with nutritional immunotherapy nanosystems for combating MRSA biofilms, Sci. Adv. 9 (2023) 9116.

[39] H.E. Stutz, K.W.M. Quixley, L.D. McMaster, S.J. Reid, Co-regulation of the nitrogen-assimilatory gene cluster in Clostridium saccharobutylicum, Microbiology 153 (2007) 3081–3090.

[40] W. Xu, K. Tian, S. Hu, M. Chen, M. Zhang, IL-9 promotes methicillin-resistant Staphylococcus aureus pneumonia by regulating the polarization and phagocytosis of macrophages, Infect. Immun. 91 (2023) 0016623.

[41] H. Zhou, X. Tan, G. Chen, X. Liu, A. Feng, Z. Liu, W. Liu, Extracellular vesicles of commensal skin microbiota alleviate cutaneous inflammation in atopic dermatitis mouse model by Re-establishing skin homeostasis, J. Invest. Dermatol. (2023). S0022-202X(23)00169.

[42] E. Gupta, S. Kumar, V.K. Srivastava, J. Saxena, A.J. Siddiqui, S. Mehta, S. Kaushik, A. Jyoti, Unravelling the differential host immuno-inflammatory responses to Staphylococcus aureus and Escherichia coli infections in sepsis, Vaccines 10 (2022) 1648.

[43] C.J. Schiffer, M. Abele, M.A. Ehrmann, R.F. Vogel, Bap-Independent biofilm formation in Staphylococcus xylosus, Microorganisms 9 (2021) 2610.

[44] T.L. Kinkel, S. Ramos-Montañez, J.M. Pando, D.V. Tadeo, E.N. Strom, S.J. Libby, F. C. Fang, An essential role for bacterial nitric oxide synthase in Staphylococcus aureus electron transfer and colonization, Nature microbiology 2 (2016) 16224.

[45] L. Matilla-Cuenca, A. Taglialegna, C. Gil, A. Toledo-Arana, I. Lasa, J. Valle, Bacterial biofilm functionalization through Bap amyloid engineering, NPJ biofilms and microbiomes 8 (2022) 62.

[46] T.E. Sutherland, D.P. Dyer, J.E. Allen, The extracellular matrix and the immune system: a mutually dependent relationship, Science 379 (2023) 8964.

[47] E. Fleischmann, R. Lenhardt, A. Kurz, F. Herbst, B. Fülesdi, R. Greif, D.I. Sessler, O. Akça, Outcomes Research Group, Nitrous oxide and risk of surgical wound infection: a randomised trial, Lancet 366 (2005) 1101–1107.

[48] R. He, C. Ding, Y. Luo, G. Guo, J. Tang, H. Shen, Q. Wang, X. Zhang, Congener-induced sulfur-related metabolism interference therapy promoted by photothermal sensitization for combating bacteria, Advanced materials 44 (2021) 2104410.

[49] I.J. McCallum, P.M. King, J. Bruce, Healing by primary closure versus open healing after surgery for pilonidal sinus: systematic review and meta-analysis, BMJ 7649 (2008) 868–871.

[50] C. Bonnans, J. Chou, Z. Werb, Remodelling the extracellular matrix in development and disease, Nat. Rev. Mol. Cell Biol. 15 (2014) 786–801.

[51] G. Guo, Z. Liu, J. Yu, Y. You, M. Li, B. Wang, J. Tang, P. Han, J. Wu, H. Shen, Neutrophil function conversion driven by immune switchpoint regulator against diabetes-related biofilm infections, Advanced materials 36 (2024) 2310320.

[52] L.M. Beaulieu, E. Lin, K.M. Morin, K. Tanriverdi, J.E. Freedman, Regulatory effects of TLR2 on megakaryocytic cell function, Blood 117 (2011) 5963–5974.

[53] Y. Wang, Y. Wu, B. Zhang, C. Zheng, C. Hu, C. Guo, Q. Kong, Y. Wang, Repair of degenerative nucleus pulposus by polyphenol nanosphere-encapsulated hydrogel gene delivery system, Biomaterials 298 (2023) 122132.

[54] F. Han, Z. Tu, Z. Zhu, D. Liu, Q. Meng, Q. Yu, Y. Wang, J. Chen, T. Liu, F. Han, B. Li, Targeting endogenous reactive oxygen species removal and regulating regenerative microenvironment at annulus fibrosus defects promote tissue repair, ACS Nano 17 (2023) 7645–7661.

[55] V. De Gregorio, C. Sgambato, F. Urciuolo, R. Vecchione, P.A. Netti, G. Imparato, Immunoresponsive microbiota-gut-on-chip reproduces barrier dysfunction, stromal reshaping and probiotics translocation under inflammation, Biomaterials 286 (2022) 121573.

[56] Z. Wang, X. Yao, R. Wang, Y. Ji, T. Yue, J. Sun, T. Li, J. Wang, D. Zhang, Label-free strip sensor based on surface positively charged nitrogen-rich carbon nanoparticles for rapid detection of Salmonella enteritidis, Biosens. Bioelectron. 132 (2019) 360–367.

[57] L. Xiao, M. Feng, C. Chen, Q. Xiao, Y. Cui, Y. Zhang, Microenvironment-regulating drug delivery nanoparticles for treating and preventing typical biofilm-induced oral diseases, Advanced materials 10 (2023) 2304982.

[58] M. Deng, M. Zhang, R. Huang, H. Li, W. Lv, X. Lin, R. Huang, Y. Wang, Diabetes immunity-modulated multifunctional hydrogel with cascade enzyme catalytic activity for bacterial wound treatment, Biomaterials 289 (2022) 121790.

[59] X. Yang, C. Xu, F. Yao, Q. Ding, H. Liu, C. Luo, D. Wang, J. Huang, Z. Li, Y. Shen, W. Yang, Z. Li, F. Yu, Y. Fu, L. Wang, Q. Ma, J. Zhu, F. Xu, X. Cong, W. Kong, Targeting endothelial tight junctions to predict and protect thoracic aortic aneurysm and dissection, Eur. Heart J. 44 (2023) 1248–1261.

[60] A. Barkaway, L. Rolas, R. Joulia, J. Bodkin, T. Lenn, C. Owen-Woods, N. Reglero-Real, M. Stein, L. Vázquez-Martínez, T. Girbl, R.N. Poston, M. Golding, R.S. Saleeb, A. Thiriot, U.H. von Andrian, J. Duchene, M.B. Voisin, C.L. Bishop, D. Voehringer,

A. Roers, S. Nourshargh, Age-related changes in the local milieu of inflamed tissues cause aberrant neutrophil trafficking and subsequent remote organ damage, Immunity 54 (2021) 1494–1510.

[61] C. Tiruppathi, D.M. Wang, M.O. Ansari, S. Bano, Y. Tsukasaki, A. Mukhopadhyay, J.C. Joshi, C. Loch, H.W.M. Niessen, A.B. Malik, Ubiquitin ligase CHFR mediated degradation of VE-cadherin through ubiquitylation disrupts endothelial adherens junctions, Nat. Commun. 14 (2023) 6582.

[62] B. Liao, L. Geng, F. Zhang, L. Shu, L. Wei, P.K.K. Yeung, K.S.L. Lam, S.K. Chung, J. Chang, P.M. Vanhoutte, A. Xu, K. Wang, R.L.C. Hoo, Adipocyte fatty acid-binding protein exacerbates cerebral ischaemia injury by disrupting the blood-brain barrier, Eur. Heart J. 41 (2020) 3169–3180.

[63] P. Lizano, S. Pong, S. Santarriaga, D. Bannai, R. Karmacharya, Brain microvascular endothelial cells and blood-brain barrier dysfunction in psychotic disorders, Mol. Psychiatr. 28 (2023) 3698–3708.

[64] M. Song, G.W. Dorn 2nd, Mitoconfusion: noncanonical functioning of dynamism factors in static mitochondria of the heart, Cell Metabol. 21 (2015) 195–205.

[65] T. Yamada, D. Murata, Y. Adachi, K. Itoh, S. Kameoka, A. Igarashi, T. Kato, Y. Araki, R.L. Huganir, T.M. Dawson, T. Yanagawa, K. Okamoto, M. Iijima, H. Sesaki, Mitochondrial stasis reveals p62-mediated ubiquitination in Parkin-independent mitophagy and mitigates Nonalcoholic fatty liver disease, Cell Metabol. 28 (2018) 588–604.

[66] J. Florido, L. Martinez-Ruiz, C. Rodriguez-Santana, A. López-Rodríguez, A. Hidalgo-Gutiérrez, C. Cottet-Rousselle, F. Lamarche, U. Schlattner, A. Guerra-Librero, P. Aranda-Martínez, D. Acuña-Castroviejo, L.C. López, G. Escames, Melatonin drives apoptosis in head and neck cancer by increasing mitochondrial ROS generated via reverse electron transport, J. Pineal Res. 73 (2022) 12824.

[67] C. Lv, W. Kang, S. Liu, P. Yang, Y. Nishina, S. Ge, A. Bianco, B. Ma, Growth of ZIF-8 nanoparticles in situ on graphene oxide nanosheets: a multifunctional nanoplatform for combined ion-interference and photothermal therapy, ACS Nano 16 (2022) 11428–11443.

[68] H. Sies, D.P. Jones, Reactive oxygen species (ROS) as pleiotropic physiological signalling agents, Nat. Rev. Mol. Cell Biol. 21 (2020) 363–383.

[69] J.O. Onukwufor, M.A. Farooqi, A. Vodičková, S.A. Koren, A. Baldzizhar, B.J. Berry, G. Beutner, G.A. Porter Jr., V. Belousov, A. Grossfield, A.P. Wojtovich, A reversible mitochondrial complex I thiol switch mediates hypoxic avoidance behavior in C. elegans, Nat. Commun. 13 (2022) 2403.

[70] G.S. Shadel, T.L. Horvath, Mitochondrial ROS signaling in organismal homeostasis, Cell 163 (2015) 560–569.